International Journal of Plasticity 27 (2011) 1677–1701

Contents lists available at ScienceDirect

International Journal of Plasticity

journal homepage: www.elsevier.com/locate/ijplas

Dual-stage nested homogenization for rate-dependent anisotropic elasto-plasticity model of dendritic cast aluminum alloys

Daniel Paquet, Piyush Dondeti, Somnath Ghosh *

Department of Mechanical Engineering, The Ohio State University, 201 West 19th Avenue, Columbus, OH 43210, USA

ARTICLE INFO

Article history:
Received 30 October 2010
Received in final revised form 21 January 2011
Available online 15 February 2011

Keywords:
Anisotropic continuum plasticity model
Rate-dependent material
LE-VCFEM
Asymptotic expansion homogenization
Self-consistent homogenization

ABSTRACT

This paper proposes a nested dual-stage homogenization method for developing microstructure based continuum elasto-viscoplastic models for large secondary dendrite arm spacing or SDAS cast aluminum alloys. Microstructures of these alloys are characterized by extremely inhomogeneous distribution of inclusions along the dendrite cell boundaries. Traditional single-step homogenization methods are not suitable for this type of microstructure due to the size of the representative volume element (RVE) and the associated computations required for micromechanical analyses. To circumvent this limitation, two distinct RVE's or statistically equivalent RVE's are identified, corresponding to the inherent scales of inhomogeneity in the microstructure. The homogenization is performed in multiple stages for each of the RVE's identified. The macroscopic behavior is described by a rate-dependent, anisotropic homogenization based continuum plasticity (HCP) model. Anisotropy and viscoplastic parameters in the HCP model are calibrated from homogenization of micro-variables for the different RVE's. These parameters are dependent on microstructural features such as morphology and distribution of different phases. The uniqueness of the nested two-stage homogenization is that it enables evaluation of the overall homogenized model parameters of the cast alloy from limited experimental data, but also material parameters of constituents like inter-dendritic phase and pure aluminum matrix. The capabilities of the HCP model are demonstrated for a cast aluminum alloy AS7GU having a SDAS of 30 μm.

© 2011 Elsevier Ltd. All rights reserved.

1. Introduction

Metals and alloys containing heterogeneities e.g. particulates, precipitates, intermetallics, or voids in the microstructure are widely used in automotive, aerospace among other engineering systems. The micrograph in Fig. 1 depicts the microstructure of a Al–Si–Mg hypoeutectic cast aluminum alloy (AS7GU) used in the automotive industry. The microstructure comprises of (i) age-hardened aluminum matrix, strengthened by Mg/Si and Si precipitates, and (ii) a dispersion of brittle silicon particulates in the matrix. The spatial distribution of the silicon inclusions and their morphology depends on the casting procedure used, and especially on the rate of heat extraction (Ghosh et al., 2006). The solidification process tends to push particulates into the regions between the evolving secondary dendrite arms. Once the eutectic temperature is reached, the silicon inclusions are pinned in location. This process results in a very inhomogeneous distribution of the Si inclusions in the microstructure as seen in Fig. 1(a). The distribution of silicon inclusions along the dendrite cell boundaries results in the delineation of two different material phases in Fig. 1(a), viz. (i) a heterogeneity-free pure aluminum matrix, and (ii) an inter-dendritic phase (IDP) in which silicon inclusions are dispersed in the aluminum matrix. The spatial distribution

* Corresponding author. Tel.: +1 614 292 2599; fax: +1 614 292 7369.
E-mail address: ghosh.5@osu.edu (S. Ghosh).

0749-6419/$ - see front matter © 2011 Elsevier Ltd. All rights reserved.
doi:10.1016/j.ijplas.2011.02.002

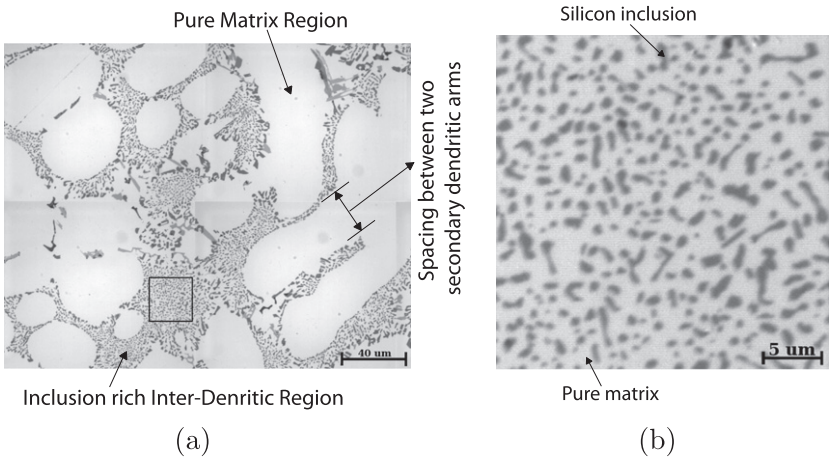

Fig. 1. (a) Micrograph of a cast aluminum alloy AS7GU (120 μm × 96 μm), (b) blow-up of the designated region in (a) (28.4 μm × 28.4 μm).

of inclusions is characterized by the distance between the secondary dendrite arms as annotated in Fig. 1(a). The average secondary dendrite arm spacing, or SDAS, of this microstructure is ∼30 μm.

Various material properties of cast aluminum alloys, such as the plastic hardening modulus, toughness, ultimate strength, and strain to failure or ductility have strong correlations to the microstructural morphology. Spatial variations of the cooling rate occur during the casting process on account of casting geometry and location of chills. This leads to variations of the microstructure in the overall structure, which consequently causes inhomogeneous material property distribution. Improvement in casting designs call for the development of physically based constitutive models that explicitly incorporate morphological descriptions of the microstructure.

A homogenization based continuum plasticity-damage (HCPD) model has been developed in Ghosh et al. (2009) for ductile failure of materials containing a dispersion of brittle inclusions. Materials like discretely reinforced aluminum (DRA's) or cast alloys, with small values of SDAS and containing precipitates and pores, can be readily modeled. The HCPD constitutive model for deformation and damage analysis of rate-independent, porous ductile materials, accounts for microstructural variations. Both, initial anisotropy due to dispersion of inclusions and deformation induced anisotropy due to nonuniform evolution of plastic strains and void distributions in the microstructure are captured. An important feature of the HCPD model is that it is represented in an evolving principal material coordinate system to account for the effects of load, deformation and damage histories on anisotropy. Anisotropy parameters (e.g. flow potential) evolve as functions of inelastic work with increasing deformation. Their functional forms are obtained by asymptotic expansion based homogenization of plasticity and damage variables from micromechanical RVE (representative volume element) analyses.

However, the model proposed in Ghosh et al. (2009) falls short in the macroscopic modeling of microstructures that contain large SDAS, as that shown in Fig. 1. A single RVE for the microstructure containing dendrites and inter-dendritic phases (IDPs), as determined by methods proposed in Swaminathan et al. (2006), Swaminathan and Ghosh (2006), Ghosh et al. (2009), may lead to dimensions exceeding the available micrograph and contain a large number of heterogeneities. This makes their simulation computationally prohibitive. Thus, it is necessary to introduce special homogenization techniques to handle the presence of heterogeneities at multiple scales. This paper proposes a novel two-stage nested homogenization scheme to circumvent this limitation. It takes benefit of the inherent multiple scales of heterogeneity present within the microstructure and eliminates the need for micromechanical analyses of a large single RVE for the entire microstructure. Instead, it identifies multiple RVE's, corresponding to the scales of microstructural heterogeneity. Two scales of heterogeneity are associated with the microstructure in Fig. 1. They are:

(1) *Length scale of intra-IDP inclusions*: The first RVE is at the scale of intra-IDP Si inclusions in the aluminum matrix as illustrated in Fig. 1(b). This scale will be referred to as the *level-1* microscopic scale. It is associated with the smaller length-scale of silicon inclusions inside the IDP.
(2) *Length scale of dendrite cells*: The second RVE is for the scale of dendrite cells in Fig. 1(a). It is associated with the larger scale of inhomogeneous dispersions in the microstructural domain containing the pure aluminum matrix in the dendrite and the inter-dendritic phases or IDPs. This scale will be referred to as the *level-2* microscopic scale.

This paper develops an anisotropic homogenization-based continuum plasticity (HCP) model for cast alloys displaying large SDAS in the microstructure, leading to two scales of heterogeneity. The HCP model is patterned after developments in Ghosh et al. (2009). However, damage evolution for ductile failure is not presented in this paper. The macroscopic HCP model parameters are calibrated from experimental stress–strain data of the aluminum alloys using a novel *dual-stage nested homogenization scheme*. Individual material properties of the aluminum matrix and Si inclusion phases may not be known *a*

priori. This is overcome by the two-stage homogenization method, which evaluates not only the macroscopic (effective) HCP model parameters that can be compared to experiments, but also constituent material properties, e.g. for the pure Al matrix and Si inclusions. The nested structure of the homogenization method is demonstrated in Fig. 2. With estimates of constituent matrix and inclusion properties, the first homogenization evaluates effective elastic–plastic material parameters of the overall IDP. Then, the overall macroscopic material parameters of the heterogeneous alloy are obtained by the second homogenization process. The difference in macroscopic HCP model predictions and experimental data is minimized to update the microstructural constituent properties of the aluminum matrix and Si inclusions in each iteration. The iterative scheme is continued until the macroscopic behavior corresponding to the current calibrated HCP parameters converges to the experimental data.

Each of the two homogenization stages requires the identification of appropriate statistically equivalent representative volume element or SERVE (Swaminathan et al., 2006; Swaminathan and Ghosh, 2006). The SERVE is an effective microstructural domain used for evaluating homogenized properties, when the microstructure does not exhibit geometric periodicity in the strictest sense. Effective methods of evaluating the SERVE has been proposed in Swaminathan et al. (2006), Swaminathan and Ghosh (2006), Ghosh et al. (2009). Homogenization is possible only if a separation of scales is valid, i.e.

$$\frac{l_i}{L_i} = \epsilon_i \ll 1 \quad i = 1,2 \tag{1}$$

where l_i and L_i are the length scales associated with the SERVE and macroscopic scales respectively, for each stage ($i = 1,2$) of homogenization.

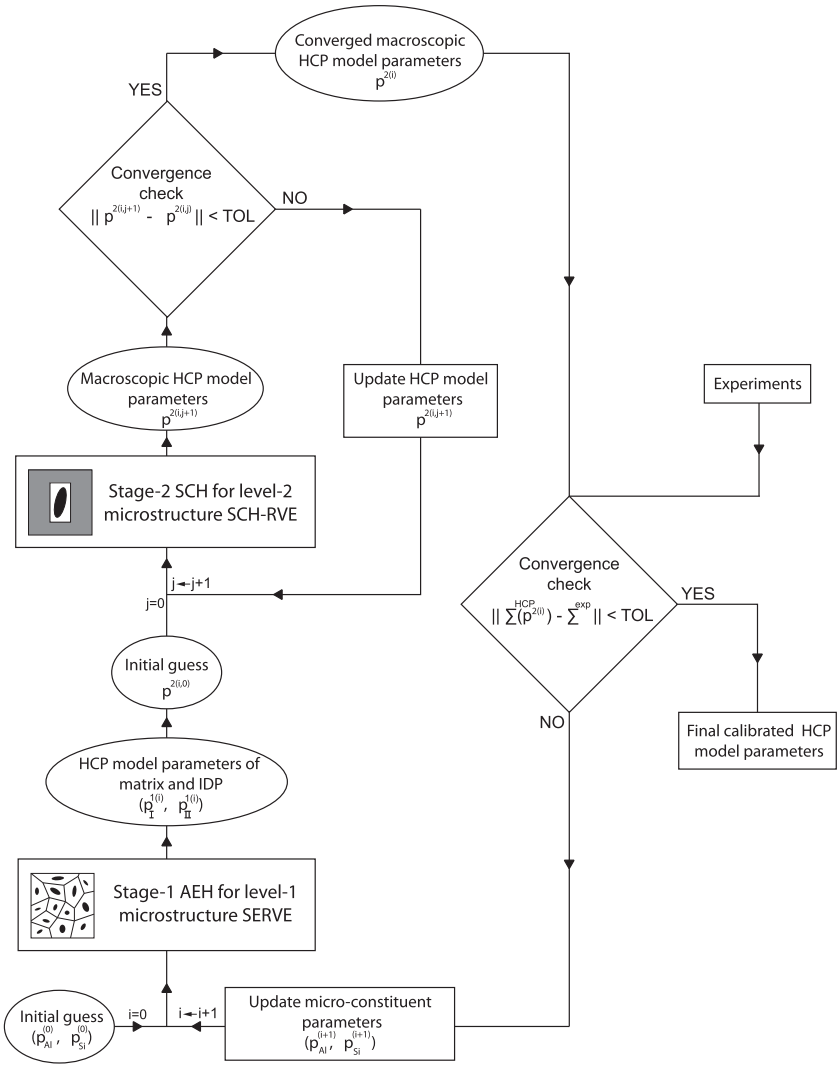

Fig. 2. Schematic flow chart of the nested two-stage homogenization method for large SDAS cast aluminum alloys.

Two different methods of homogenization or bottom-up coupling are used sequentially in the nested homogenization model of Fig. 2. They are:

(*i*) *Asymptotic expansion-based homogenization (AEH) of level-1 microstructure containing Si inclusions in intra-IDP RVE's*: The stage-1 homogenization develops an effective elastic–plastic constitutive model for the Si particle-rich, ID region shown in the box of Fig. 1(a) and in Fig. 1(b). Asymptotic expansion-based homogenization has been demonstrated to be quite effective for elastic–plastic constitutive modeling of this type of microstructure in Ghosh et al., 1996, 2009. The micro-scale problem involves identification of a SERVE (Swaminathan et al., 2006; Swaminathan and Ghosh, 2006; Ghosh et al., 2009) and subsequent micromechanical analyses with the *locally enhanced Voronoi cell finite element method* (LE-VCFEM) (Hu and Ghosh, 2008; Paquet and Ghosh, 2011a). Parameters of the HCP model are calibrated from homogenization of evolving variables in the SERVE.

(*ii*) *Self-consistent homogenization (SCH) of level-2 microstructure containing dendrites and IDPs*: Stage-2 homogenization generates an effective HCP constitutive model for the overall alloy microstructure, containing (i) dendritic cells of pure aluminum matrix and (ii) inclusion-rich IDP regions, as shown in Fig. 1(a). It is important to note that this model can be directly validated by experiments on the cast aluminum alloy. Stage-2 homogenization incorporates a self-consistent scheme that equilibrates a representative dendrite cell and its neighboring IDP in the overall microstructure of the alloy. It uses the constitutive laws derived from stage-1 homogenization. Self-consistent models assume no spatial correlation at the microstructural scale and hence admit complete scale separation, i.e. $\epsilon = \frac{l}{L} = 0$. Each heterogeneity sees the rest of the medium as a homogeneous material having yet undetermined macroscopic properties (Budiansky, 1965; Hill, 1965; Nemat-Nasser and Hori, 1999). Since the RVE is significantly simpler for this stage, boundary value problems are solved by conventional finite element method (FEM).

A schematic of the nested dual-stage homogenization scheme, implementing asymptotic expansion-based homogenization (AEH) and self-consistent homogenization (SCH) is shown in Fig. 2. The structure of the paper is as follows. Section 2 details the experimental methods used to characterize the microstructure and the rate-dependent plastic behavior of cast aluminum alloy AS7GU. The HCP model is discussed for rate-dependent elastic–viscoplastic heterogeneous materials in Section 3. The proposed dual-stage homogenization scheme used for calibrating the HCP model parameters is described in Section 4 and the calibration procedure is presented in Section 5. Finally, the HCP model is used to simulate rate-dependent plastic behavior of the cast aluminum alloy AS7GU in Section 6.

2. Experimental methods of material characterization

The material, provided by Ford Research Laboratory (FRL), is a hypoeutectic Al–Si–Mg cast aluminum alloy. The chemical composition is given in Table 1. Bars of dimension $18 \times 35 \times 150$ mm^3 are extracted from larger plates fabricated by a spatial solidification procedure to create gradients in the microstructure. The process induces differential cooling rates along their length by using a copper chill to remove heat from one end. The cooling-rate gradient results in a variation of the microstructure along their length as shown in Fig. 3(a).

2.1. Microstructure characterization

The series of micrographs in Fig. 3(a) shows the cast alloy microstructure, extracted at different distances from the copper chill. The microstructure varies significantly with different cooling rates at different distances from the chill. This variation is quantified in Fig. 4, with the secondary dendrite arm spacing (SDAS) varying linearly with distance. In addition to affecting the SDAS, the cooling rate has a significant influence on the morphology of the silicon inclusions, especially on their size. Higher cooling rates result in more refined microstructures containing smaller inclusions. Fig. 3(b) and (c) show magnified scanning electron microscopy images of the microstructures located at 4 mm and 31 mm from the chill. These are labeled as A and B in Fig. 3(a).

2.2. Mechanical characterization

The mechanical behavior of the alloy is experimentally characterized for specimens at two different locations A and B in Fig. 3(a). Compression and tensile tests are conducted to study the influence of the microstructure on mechanical properties, such as plastic work-hardening and strain to failure, at different temperatures and applied strain rates. A complete

Table 1
Chemical composition of cast aluminum alloy AS7GU (wt.%).

% Composition	Al	Si	Cu	Mg	Fe	Mn	Sr	Ti
Minimum	92.625	6.50	0.40	0.30	-	0.05	0.025	0.10
Maximum	90.91	7.50	0.60	0.45	0.20	0.10	0.040	0.20

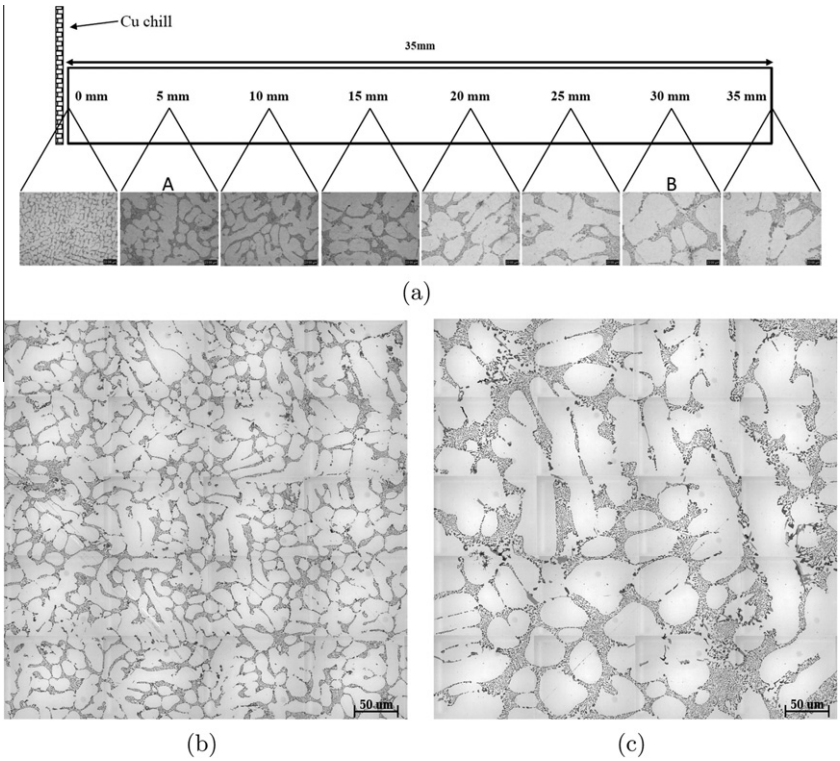

Fig. 3. (a) Micrographs at different distances from the copper chill (same magnification), (b) 236 μm × 236 μm micrograph at location A, 4 mm away from the chill, and (c) 236 μm × 236 μm micrograph at location B, 31 mm away from the chill.

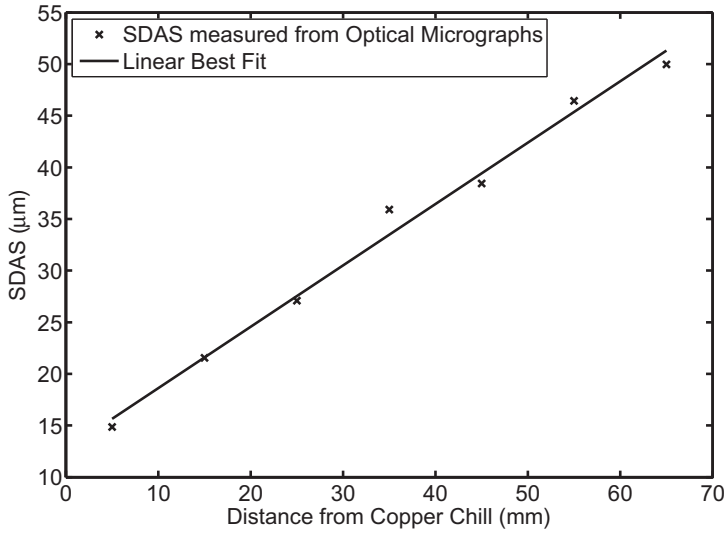

Fig. 4. Variation of secondary dendrite arm spacing (SDAS) with the distance from the copper chill (Data courtesy of Ford Research Laboratory).

description of the experimental tests performed is provided in the B.S. thesis (Chisaka, 2009). The experiments described in this paper are limited to those used for the calibration of the rate-dependent plasticity parameters of the HCP model of Section 3.

The viscoplastic behavior of the alloy at room temperature is investigated by performing compression tests on a MTS hydraulic testing machine. Cylindrical specimens are machined from the bars at locations A and B as indicated in Fig. 3(a). The corresponding microstructures are shown in Fig. 3(b) and (c). The sample geometries follow the ASTM

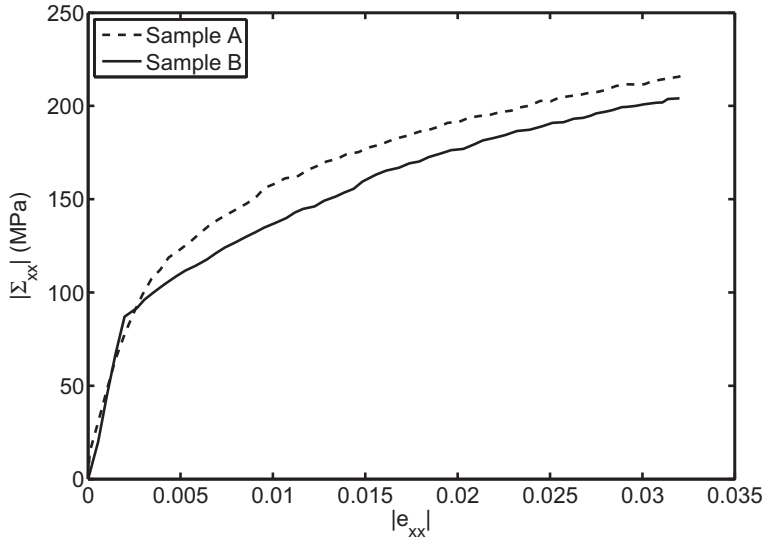

Fig. 5. Compression tests results for samples A and B for an applied strain rate $\dot{e}_{xx}^{(1)} = -0.01\ s^{-1}$.

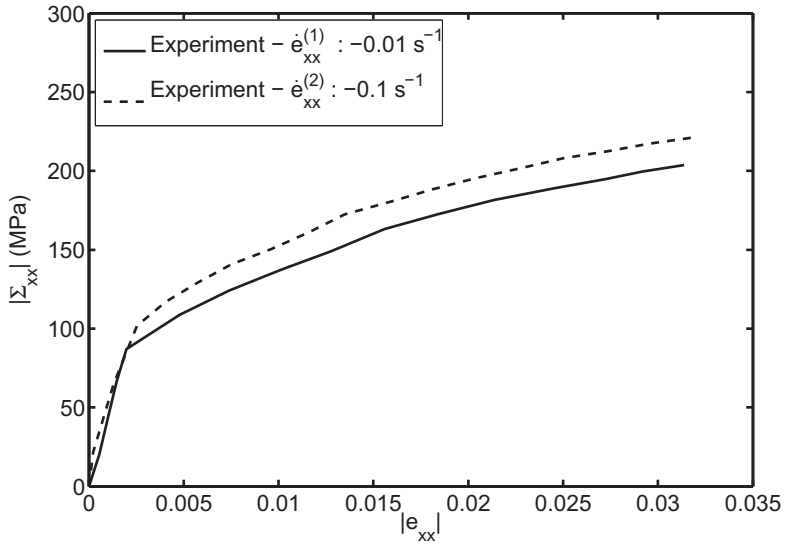

Fig. 6. Compression tests results for sample B for applied strain rates $\dot{e}_{xx}^{(1)} = -0.01\ s^{-1}$ and $\dot{e}_{xx}^{(2)} = -0.1\ s^{-1}$.

E209-00 standard and have longitudinal and diameter dimensions of 8.61 mm and 2.87 mm, respectively. The first set of compression tests are conducted at a very low strain rate $\dot{e}_{xx}^{(1)} = -0.01\ s^{-1}$ to investigate the influence of the microstructure on the rate-independent plastic behavior. Experimental results, plotted in Fig. 5, show significant effect of the microstructure on work-hardening. Results associated with location B are used in Section 6.1 to calibrate the rate-independent parameters of the HCP model. The second test is performed at a strain rate $\dot{e}_{xx}^{(2)} = -0.1\ s^{-1}$ for sample B to study the effect of loading strain rate on the plastic behavior. From the experimental results in Fig. 6, it is observed that the loading strain rate significantly affects the plastic response. This result is used to calibrate the rate-dependence in HCP parameters in Section 6.2.

3. Homogenization based continuum plasticity model (HCP) for rate-dependent heterogeneous materials

An anisotropic rate-dependent elasto-viscoplasticity framework is assumed for the macroscopic homogenization based continuum plasticity (HCP) model. The same HCP model framework is used to represent the effective behavior of the pure matrix and inter-dendritic phases in the stage-1 homogenization, as well as of the overall cast alloy in the stage-2 homogenization. However the parameters and the evolution laws are different for these different phases. Previous studies in Ghosh et al. (2009) and Garajeu and Suquet (1997) have demonstrated conclusively that this assumption of the same

overall framework for modeling the constituent plastic phase and overall material behavior is quite effective for heterogeneous materials with brittle inclusions. In this constitutive model, the total strain rate is assumed to admit an additive decomposition into an elastic and viscoplastic part as:

$$\dot{\mathbf{e}} = \dot{\mathbf{e}}^{\mathbf{e}} + \dot{\mathbf{e}}^{\mathbf{p}} \tag{2}$$

For small elastic strains, the rate of Cauchy stress $\dot{\boldsymbol{\Sigma}}$ is related to the elastic part of the strain rate tensor as: $\dot{\boldsymbol{\Sigma}} = \mathbf{C}^{\mathbf{e}} : \dot{\mathbf{e}}^{\mathbf{e}}$, where $\mathbf{C}^{\mathbf{e}}$ is a fourth order anisotropic elasticity tensor. Rate dependency is introduced through an over-stress viscoplastic model, developed by Perzyna (1966). In this model, the viscoplastic strain rate is expressed in terms of a function $\Phi(F)$ of the over-stress F as (see Ghosh and Kikuchi, 1991):

$$\dot{\mathbf{e}}^{\mathbf{p}} = \Gamma_0 \Phi(F) \frac{\partial F/\partial \boldsymbol{\Sigma}}{\|\partial F/\partial \boldsymbol{\Sigma}\|} \tag{3}$$

where Γ_0 is a temperature dependent viscosity coefficient. The viscoplastic strain rate in Eq. (3) follows the associated flow rule and hence satisfies normality and incompressibility conditions. In Perzyna (1966) and Ghosh and Kikuchi (1991) a power law expression, i.e. $\Phi(F) = \langle F \rangle^P$ has been discussed to adequately represent the behavior of most metals. $\langle\ \rangle$ is the Mac-Cauley operator corresponding to the positive sign of the argument. The over-stress F corresponds to a measure of the excess stress over the rate-independent local yield strength Y_f (an internal state variable), i.e.

$$F = \Sigma_{eq} - Y_f(W_p) \tag{4}$$

The effect of strain work-hardening is incorporated by expressing the yield strength Y_f as a function of the macroscopic plastic work W_p. The functional form of this yield strength is determined from the homogenization process. Since this paper focuses on material ductility under monotonic loading conditions, only isotropic hardening is considered in the HCP model. Other forms of hardening, e.g. kinematic hardening may be required if it is extended to more complex loading conditions, such as cyclic loading.

As discussed in Ghosh et al. (2009), initial macroscopic material anisotropy is due to the presence of heterogeneities, e.g. brittle inclusions, in the microstructure. Furthermore, this anisotropy evolves with deformation due to nonuniform and constrained plastic flow in micro-channels between heterogeneities. The equivalent stress Σ_{eq} in the over-stress expression (4) is designed to accommodate both initial and evolving anisotropy. For plane strain (or plane stress) problems, it is expressed using the anisotropic yield function in Hill (1948) as:

$$\Sigma_{eq}^2 = F(\Sigma_{yy} - \Sigma_{zz})^2 + G(\Sigma_{zz} - \Sigma_{xx})^2 + H(\Sigma_{xx} - \Sigma_{yy})^2 + C\Sigma_{xy}^2 \tag{5}$$

The stress components (and other tensor variables) in the anisotropic constitutive relations are represented in the principal axes of material anisotropy. The material is assumed to remain orthotropic in this system throughout the deformation process. The use of this material coordinate system has been shown in Ghosh et al. (2009) to capture the effects of non-proportional load and deformation histories with very good accuracy. The angle β, delineating the principal axes of anisotropy for plane strain (or plane stress) analysis, is determined in every increment from the condition that the transformed tangent modulus $\left(E_{ijkl}^{\tan}\right)'$ in this system remains orthotropic. This condition renders the terms coupling normal and shear components of the tangent modulus to be equal to zero, i.e.

$$\left(E_{1112}^{\tan}\right)' = \left(E_{2212}^{\tan}\right)' = \left(E_{3312}^{\tan}\right)' = 0, \tag{6}$$

where $\left(E_{ijkl}^{\tan}\right)' = Q_{im}Q_{jn}Q_{kp}Q_{lq}E_{mnpq}^{\tan}$ and

$$[\mathbf{Q}] = \begin{bmatrix} \cos\beta & \sin\beta & 0 \\ -\sin\beta & \cos\beta & 0 \\ 0 & 0 & 1 \end{bmatrix}$$

Anisotropy parameters F, G, H, and C in Eq. (5) are calibrated with respect to this principal coordinate system from homogenization. These parameters evolve due to the constrained plastic flow resulting from the presence of heterogeneities. The conventional assumption of constant plasticity parameters in Liao et al. (1997), Wang et al. (2004), Benzerga et al. (2004) is therefore inappropriate for heterogeneous microstructures.

4. Dual-stage homogenization for large SDAS cast alloys

The dual-stage nested homogenization discussed in Section 1 involves both asymptotic expansion-based homogenization (stage-1) and self-consistent homogenization (stage-2). The following subsections provide a brief summary of these methods.

4.1. Asymptotic expansion-based homogenization (AEH) for level-1 microstructure

The first stage in Fig. 2 evaluates the HCP material parameters of the inter-dendritic phase (IDP) using the asymptotic expansion-based homogenization or AEH theory. The AEH theory was proposed in Benssousan et al., 1978, Sanchez-Palencia (1983) and Auriault (2002) and has been developed for elasticity and plasticity of heterogeneous materials in Ghosh et al. (1995, 1996, 2001, 2007, 2009). AEH is used to decouple the elastic–viscoplastic governing equations for the microstructure into two sets, viz.:

(i) *level-1* microscopic governing equations at the length scale l_1 of intra-IDP inclusions in Fig. 1(b), where the resolution corresponds to individual Si inclusions and aluminum matrix;
(ii) *level-2* microscopic governing equations at the length scale L_1 of the microstructure shown in Fig. 1(a) with dendrites and IDPs as the principal constituents.

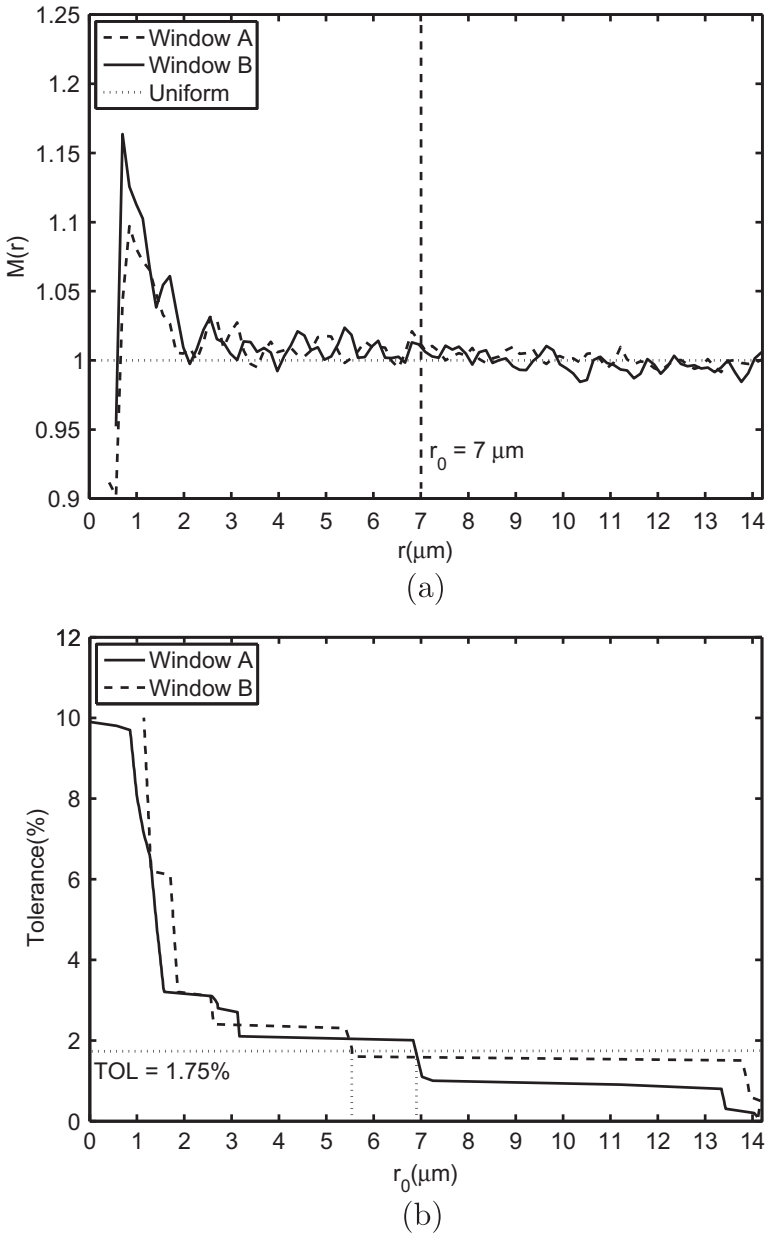

Fig. 7. (a) Marked correlation function for two different windows A and B using the mark of Eq. (31), (b) radius of convergence r_0 based on the results of (a) as a function of the chosen tolerance.

The scale l_1 of the intra-IDP SERVE is typically very small in comparison with the overall dimension L_1 of the alloy microstructure. Correspondingly the level-1 microscopic coordinates $\mathbf{y}$ in the SERVE $Y(\mathbf{x})$ are related to level-2 microscopic coordinates $\mathbf{x}$ as: $\mathbf{y} = \frac{\mathbf{x}}{\epsilon_1}$. $\epsilon_1 \ll 1$ is a small positive number representing the ratio of the length scales. Ω^ϵ denotes a connected domain that extends the microstructural domain to the intra-IDP level-1 microstructure, i.e.

$$\Omega^\epsilon = \left\{ \mathbf{x} \in \Omega : \Theta\left(\frac{\mathbf{x}}{\epsilon_1}\right) = 1 \right\} \tag{7}$$

in which $\Theta(\mathbf{y}) = 1$ when $\mathbf{y}$ lies in the SERVE $Y(\mathbf{x})$. Superscript ϵ denotes association with both length scales $(\mathbf{x},\mathbf{y})$.

When subjected to body forces, surface tractions and applied displacements, the resulting response variables like deformation and stresses vary from point to point in the *level-2* microscopic scale $\mathbf{x}$. Furthermore, the high level of intra-IDP heterogeneity causes a rapid variation of these variables in a small neighborhood ϵ of a point $\mathbf{x}$. Thus, all quantities have two explicit dependences; one on the *level-2* scale $\mathbf{x}$ and the other on the *level-1* microscopic scale $\mathbf{y}$. This association of any response function with both length scales leads to the relation $f^\epsilon(\mathbf{x}) = f(\mathbf{x},\mathbf{y})$. In addition, an assumed Y-periodicity of the function in the SERVE is expressed as $f(\mathbf{x},\mathbf{y}) = f(\mathbf{x},\mathbf{y} + \mathbf{kY})$, where $\mathbf{Y}$ is a translation vector characterizing Y-periodicity of the RVE and $\mathbf{k}$ in 2D represents a 2×2 array of integers. The spatial derivative of f^ϵ associated with two length scales is given as:

$$\frac{\partial f^\epsilon}{\partial \mathbf{x}} = \frac{\partial f}{\partial \mathbf{x}} + \frac{1}{\epsilon_1}\frac{\partial f}{\partial \mathbf{y}} \tag{8}$$

It is assumed that the stress and displacement fields satisfy the following rate-dependent governing equations:

$$\underline{\text{Equilibrium}} \quad \frac{\partial \dot{\boldsymbol{\sigma}}^\epsilon}{\partial \mathbf{x}} + \dot{\mathbf{f}} = 0 \quad \text{in } \Omega^\epsilon \tag{9}$$

$$\underline{\text{Kinematic Relation}} \quad \dot{\boldsymbol{\epsilon}}^\epsilon = \frac{1}{2}\left[\left(\frac{\partial \dot{\mathbf{u}}^\epsilon}{\partial \mathbf{x}}\right) + \left(\frac{\partial \dot{\mathbf{u}}^\epsilon}{\partial \mathbf{x}}\right)^T\right] \quad \text{in } \Omega^\epsilon \tag{10}$$

$$\underline{\text{Constitutive Relation}} \quad \dot{\boldsymbol{\sigma}}^\epsilon = \mathbf{E}^\epsilon_{\text{tan}}\dot{\boldsymbol{\epsilon}}^\epsilon \quad \text{in } \Omega^\epsilon \tag{11}$$

$\mathbf{u}^\epsilon = \mathbf{u}(\mathbf{x},\mathbf{y})$ is the displacement field, $\boldsymbol{\sigma}^\epsilon$ and $\boldsymbol{\epsilon}^\epsilon$ are the stress and strain tensors, $\mathbf{E}^\epsilon_{\text{tan}}$ is the elastic–viscoplastic tangent modulus, and $\mathbf{f}$ is the body force vector. Furthermore the prescribed boundary conditions on the traction boundary Γ_t and displacement boundary Γ_u are respectively:

$$\dot{\mathbf{u}}^\epsilon = \dot{\bar{\mathbf{u}}} \quad \text{on } \Gamma_u \quad \text{(Displacement bc's)} \tag{12}$$

$$\dot{\boldsymbol{\sigma}}^\epsilon \cdot \mathbf{n} = \dot{\bar{\mathbf{t}}} \quad \text{on } \Gamma_t \quad \text{(Traction bc's)} \tag{13}$$

where $\mathbf{n}$ is the unit normal to the boundary.

AEH methods expand solution fields in the RVE, e.g. displacement field $\mathbf{u}^\epsilon(\mathbf{x})$ and stress field $\boldsymbol{\sigma}^\epsilon(\mathbf{x})$ about their respective macroscopic values. In mathematical homogenization theory, the displacement rate field is asymptotically expanded about $(\mathbf{x})$ with respect to the parameter ϵ_1 as:

$$\dot{\mathbf{u}}^\epsilon(\mathbf{x}) = \dot{\mathbf{u}}^0(\mathbf{x},\mathbf{y}) + \epsilon_1\dot{\mathbf{u}}^1(\mathbf{x},\mathbf{y}) + \epsilon_1^2\dot{\mathbf{u}}^2(\mathbf{x},\mathbf{y}) + \cdots \tag{14}$$

The Y-periodic displacement increments are applied on ∂Y. This results in Y-anti-periodic tractions on ∂Y and hence there are no traction boundaries applied. The asymptotic expansion of the displacement rate gradient is of the form:

$$\frac{\partial \dot{\mathbf{u}}^\epsilon(\mathbf{x})}{\partial \mathbf{x}} = \frac{1}{\epsilon_1}\frac{\partial \dot{\mathbf{u}}^0}{\partial \mathbf{y}} + \left[\frac{\partial \dot{\mathbf{u}}^0}{\partial \mathbf{x}} + \frac{\partial \dot{\mathbf{u}}^1}{\partial \mathbf{y}}\right] + \epsilon_1\left[\frac{\partial \dot{\mathbf{u}}^1}{\partial \mathbf{x}} + \frac{\partial \dot{\mathbf{u}}^2}{\partial \mathbf{y}}\right] + \cdots \tag{15}$$

Substituting Eq. (15) into the kinematic Eq. (10) and using the constitutive relation Eq. (11) yield the following expression for the rate of stress tensor:

$$\dot{\boldsymbol{\sigma}}^\epsilon = \frac{1}{\epsilon_1}\dot{\boldsymbol{\sigma}}^0(\mathbf{x},\mathbf{y}) + \dot{\boldsymbol{\sigma}}^1(\mathbf{x},\mathbf{y}) + \epsilon_1\dot{\boldsymbol{\sigma}}^2(\mathbf{x},\mathbf{y}) + \cdots \tag{16}$$

where

$$\dot{\boldsymbol{\sigma}}^0(\mathbf{x},\mathbf{y}) = \mathbf{E}^\epsilon_{\text{tan}}\frac{1}{2}\left[\left(\frac{\partial \dot{\mathbf{u}}^0}{\partial \mathbf{y}}\right) + \left(\frac{\partial \dot{\mathbf{u}}^0}{\partial \mathbf{y}}\right)^T\right] \tag{17}$$

$$\dot{\boldsymbol{\sigma}}^1(\mathbf{x},\mathbf{y}) = \mathbf{E}^\epsilon_{\text{tan}}\frac{1}{2}\left[\left(\frac{\partial \dot{\mathbf{u}}^0}{\partial \mathbf{x}}\right) + \left(\frac{\partial \dot{\mathbf{u}}^0}{\partial \mathbf{x}}\right)^T + \left(\frac{\partial \dot{\mathbf{u}}^1}{\partial \mathbf{y}}\right) + \left(\frac{\partial \dot{\mathbf{u}}^1}{\partial \mathbf{y}}\right)^T\right] \tag{18}$$

$$\dot{\boldsymbol{\sigma}}^2(\mathbf{x},\mathbf{y}) = \mathbf{E}^\epsilon_{\text{tan}}\frac{1}{2}\left[\left(\frac{\partial \dot{\mathbf{u}}^1}{\partial \mathbf{x}}\right) + \left(\frac{\partial \dot{\mathbf{u}}^1}{\partial \mathbf{x}}\right)^T + \left(\frac{\partial \dot{\mathbf{u}}^2}{\partial \mathbf{y}}\right) + \left(\frac{\partial \dot{\mathbf{u}}^2}{\partial \mathbf{y}}\right)^T\right] \tag{19}$$

Introducing Eq. (16) into the equilibrium Eq. (9) and arranging terms with the same exponent p of $\epsilon_1 (p = -2, -1, 0, \ldots)$, results in two sets of decoupled governing equations for the level-1 and level-2 micro-scales (Ghosh et al., 2001):

Level-1 microscopic governing equations

$$\frac{\partial \dot{\boldsymbol{\sigma}}^1(\mathbf{x},\mathbf{y})}{\partial \mathbf{y}} = 0 \quad \text{(Equilibrium)} \tag{20}$$

$$\dot{\boldsymbol{\sigma}}^1(\mathbf{x},\mathbf{y}) = \mathbf{E}^{\epsilon}_{\text{tan}}(\mathbf{x},\mathbf{y})\dot{\boldsymbol{\epsilon}}(\mathbf{x},\mathbf{y}) \quad \text{(Constitutive)} \tag{21}$$

$$\dot{\boldsymbol{\epsilon}}(\mathbf{x},\mathbf{y}) = \left(\mathbf{T} + \frac{\partial \boldsymbol{\chi}(\mathbf{y})}{\partial \mathbf{y}}\right)\frac{\partial \dot{\mathbf{u}}^0(\mathbf{x})}{\partial \mathbf{x}} \quad \text{(Kinematics)} \tag{22}$$

Level-2 microscopic governing equations

$$\frac{\partial \dot{\boldsymbol{\Sigma}}(\mathbf{x})}{\partial \mathbf{x}} + \dot{\mathbf{f}}(\mathbf{x}) = 0 \quad \text{(Equilibrium)} \tag{23}$$

$$\dot{\boldsymbol{\Sigma}}(\mathbf{x}) = \mathbf{E}^{H}_{\text{tan}}(\mathbf{x})\dot{\mathbf{e}}(\mathbf{x}) \quad \text{(Constitutive)} \tag{24}$$

$$\dot{\mathbf{e}}(\mathbf{x}) = \frac{1}{2}\left[\left(\frac{\partial \dot{\mathbf{u}}^0(\mathbf{x})}{\partial \mathbf{x}}\right) + \left(\frac{\partial \dot{\mathbf{u}}^0(\mathbf{x})}{\partial \mathbf{x}}\right)^T\right] \quad \text{(Kinematics)} \tag{25}$$

$$\dot{\mathbf{u}}^0 = \dot{\bar{\mathbf{u}}} \quad \text{on } \Gamma_u \quad \text{(Displacement bc's)} \tag{26}$$

$$\dot{\boldsymbol{\Sigma}} \cdot \mathbf{n} = \dot{\bar{\mathbf{t}}} \quad \text{on } \Gamma_t \quad \text{(Traction bc's)} \tag{27}$$

where $\boldsymbol{\chi}$ is a Y-periodic third order tensor that represents the effect of microstructure on the distribution of microscopic strains within the RVE and possesses the symmetry $\chi_i^{kl} = \chi_i^{lk}$. $\mathbf{T}$ is a fourth order identity tensor defined as $T_{ij}^{kl} = \frac{1}{2}(\delta_{ik}\delta_{jl} + \delta_{il}\delta_{jk})$. $\dot{\boldsymbol{\Sigma}} = \langle \dot{\boldsymbol{\sigma}}^1 \rangle$ is the volume average of the rate of level-1 microscopic stress tensor and $\dot{\mathbf{e}} = \langle \dot{\boldsymbol{\epsilon}} \rangle$ is the volume average of the rate of level-1 microscopic strain tensor. These results only hold if the level-1 microscopic tangent modulus $\mathbf{E}^{\epsilon}_{\text{tan}}$ is positive definite. In this case, the level-2 microscopic tangent modulus $\mathbf{E}^{H}_{\text{tan}}$ is also positive definite and is expressed as:

$$\mathbf{E}^{H}_{\text{tan}} = \frac{1}{|\mathbf{Y}|}\int_Y \mathbf{E}^{\epsilon}_{\text{tan}}\left(\mathbf{T} + \frac{\partial \boldsymbol{\chi}}{\partial \mathbf{y}}\right)\mathrm{d}Y \tag{28}$$

4.1.1. Numerical implementation of AEH for stage-1 homogenization

Stage-1 homogenization implements the asymptotic expansion-based homogenization, with results of micromechanical analyses on the SERVE for the inter-dendritic phase. Three specific tasks are executed for this purpose. These are discussed next.

I. Identification of the statistically equivalent RVE or SERVE:

Identification of the microstructural SERVE is important in the determination of effective material properties of a heterogeneous domain, e.g. the inter-dendritic region of Fig. 1(b). A SERVE may be defined as the smallest volume element of the microstructure exhibiting the following characteristics (Swaminathan et al., 2006; Swaminathan and Ghosh, 2006):

- Effective material properties in the SERVE should be equivalent to properties of the entire microstructure, at least locally to within a prescribed tolerance.
- Distribution functions of parameters reflecting the local morphology (local volume fraction, neighbor distance or radial distributions) in the SERVE should be equivalent to those for the overall microstructure.
- SERVE should be independent of the location in the local microstructure as well as of the applied loading direction.

Various methods for the determination of the SERVE size has been developed for undamaged and damaging heterogeneous solids in Swaminathan et al. (2006) and Swaminathan and Ghosh (2006). In Ghosh et al. (2009) the marked correlation function $M(r)$ has been used to establish the SERVE for porous ductile materials with a dispersion of heterogeneities. Originally introduced by Pyrz (1994), the marked correlation function $M(r)$ is a multivariate characteristic function of the microstructure that relates any field variable (either geometric or response) with the microstructural morphology. It is expressed in terms of the field variable dependent function $h(r)$ and the pair distribution function $g(r)$ as:

$$M(r) = \frac{h(r)}{g(r)} \tag{29}$$

where

$$h(r) = \frac{1}{2\pi r}\frac{\mathrm{d}H(r)}{\mathrm{d}r} \quad \text{and } H(r) = \frac{1}{m^2}\frac{A}{N^2}\sum_{i=1}^{N}\sum_{k=1}^{k_i} m_i m_k(r) \tag{30}$$

Here m_i is a mark associated with the ith inclusion, r is a measure of the radial distance of influence, $m_k(r)$ corresponds to the mark associated with the kth inclusion at a radial distance r and m is the mean of all marks. N is the total number of

inclusions within the area A of the microstructural domain being analyzed and k_i is the number of inclusions that have their center within a circle of radius r centered at the ith inclusion. The mark can be any chosen variable field in the microstructure that has relevance to a physical property being pursued. The definition of the pair distribution function $g(r)$ in Eq. (29) is given in Swaminathan et al. (2006). A high value of $M(r)$ indicates a strong correlation between entities in the microstructure. As discussed in Ghosh et al. (1997a,b), $M(r)$ provides a good estimate of the size of the SERVE, corresponding to the region of influence in the microstructure. It stabilizes to near-unity values at a characteristic radius of convergence r_0. For $r \geqslant r_0$, $M(r) \approx 1$ and the local morphology ceases to have any significant influence on the field variables beyond this characteristic radial distance. The radius r_0 corresponds to a local correlation length that provides an estimate for the SERVE size.

A combination of three geometric parameters has been suggested in Swaminathan et al. (2006) to calculate the SERVE size of the microstructure. The mark is defined as a weighted average of local area fraction (LAF), inverse near neighbor distance (IND) and the number of near neighbors (NN):

$$m_k = w_1 S_1^k + w_2 S_2^k + w_3 S_3^k \tag{31}$$

with

$$S_1^k = \frac{(LAF)^k}{\max_{1\leqslant j\leqslant N}(LAF)^j}; \quad S_2^k = \frac{(IND)^k}{\max_{1\leqslant j\leqslant N}(IND)^j}; \quad S_3^k = \frac{(NN)^k}{\max_{1\leqslant j\leqslant N}(NN)^j}$$

where N is the total number of inclusions and $(LAF)^k$, $(IND)^k$, and $(NN)^k$ are the local area fraction, the inverse of the near-neighbor distance, and the number of near-neighbors of the kth inclusion.

Two different square windows are chosen from the IDP microstructure. One of these selected regions is shown in Fig. 1(b). The marked correlation function in Eq. (29) is calculated with the geometric mark of Eq. (31) for the two windows. Weights $w_1 = 1.0$, $w_2 = 2.0$ and $w_3 = 1.0$ are used, as suggested in Swaminathan et al. (2006). $M(r)$ distributions are plotted in Fig. 7(a), showing the convergence to $M(r) = 1$ with varying r. The size of the SERVE corresponding to different acceptable tolerances

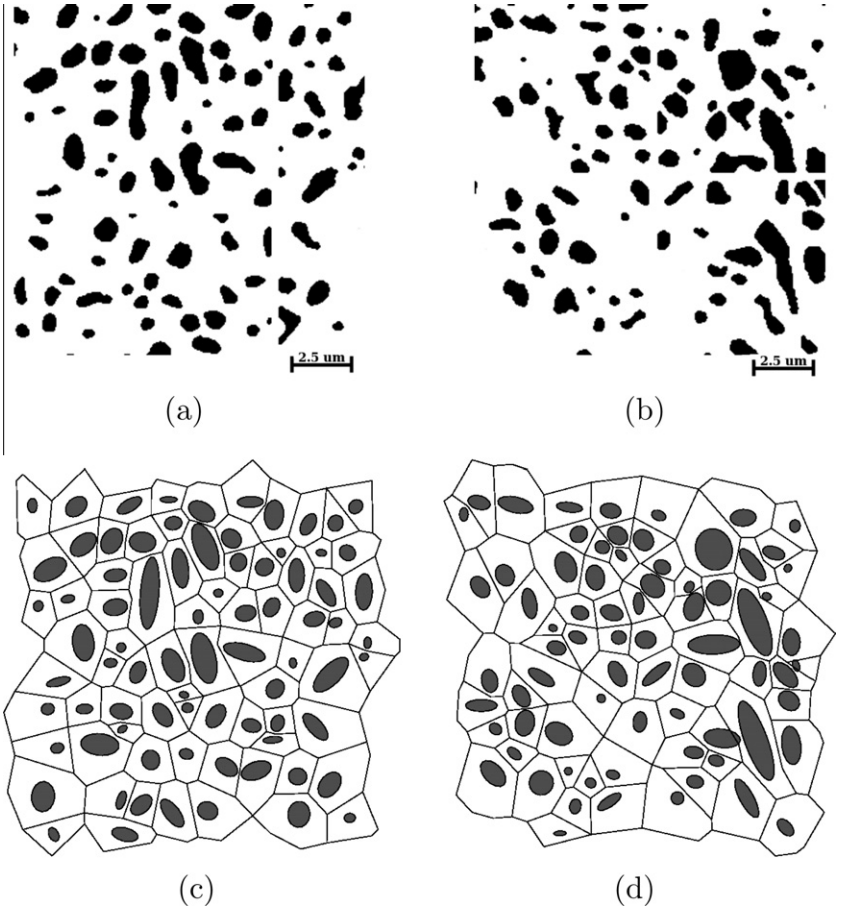

Fig. 8. (a) Micrograph of the microstructural domain of SERVE A, (b) micrograph of the microstructural domain of SERVE B, (c) SERVE A with periodic boundary, (d) SERVE B with periodic boundary.

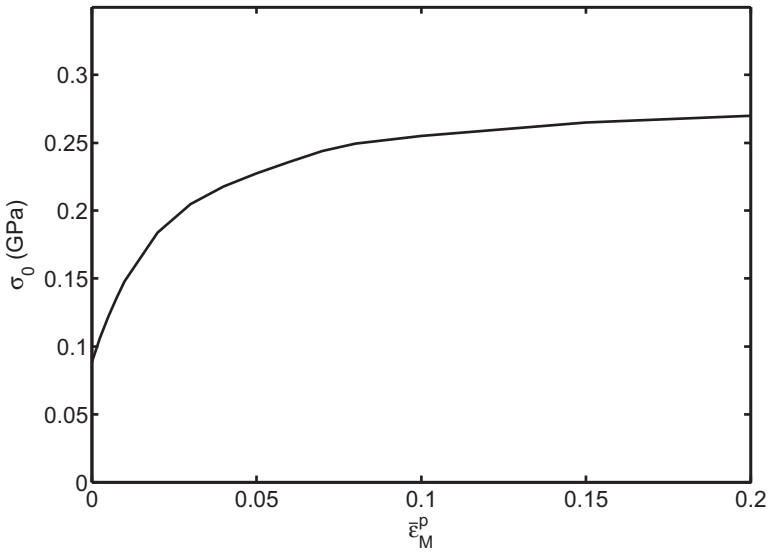

Fig. 9. Hardening (stress–strain) curve for the aluminum matrix used for comparison of macroscopic behavior in shear for SERVE A and SERVE B of Fig. 8.

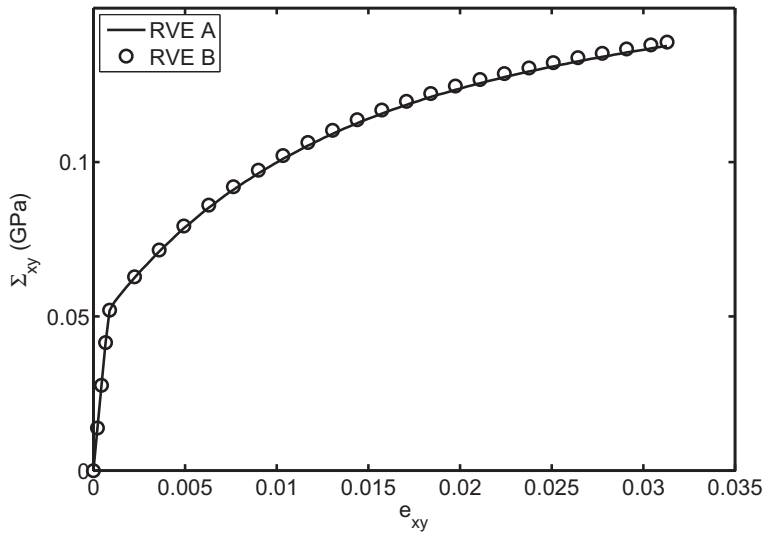

Fig. 10. Comparison of the averaged macroscopic stress–strain response in shear of SERVE A and SERVE B of Fig. 8.

for convergence are evaluated in Fig. 7(b). This analysis suggests $r_0 \approx 7$ μm based on the highest value for the two regions using a tolerance of 1.75%. Correspondingly, the SERVE size is estimated as $L_{SERVE} = 2 \times r_0$, which gives $L_{SERVE} = 14$ μm.

Location independence of the 14 μm SERVE is verified by extracting SERVE's from the two selected windows in the microstructure and comparing their respective homogenized response for rate-independent shear loading. The SERVE boundaries are created by periodically repeating the position of inclusions in the x and y directions, followed by tessellation (Ghosh and Mukhopadhyay, 1991; Raghavan and Ghosh, 2004a,b). The resulting SERVE's with the Voronoi cell mesh are shown in Fig. 8. Their respective area fraction of inclusions are 18.31% and 18.45%, which are very close to the overall area fraction of the microstructural region of Fig. 1(b) (18.62%). The elastic properties considered for micromechanical simulations are $E_{Si} = 165$ GPa and $\nu_{Si} = 0.27$ for the inclusions and $E_{Al} = 70$ GPa and $\nu_{Al} = 0.32$ for the matrix. The plastic hardening curve of the matrix is shown in Fig. 9 and the initial yield stress is $\sigma_y = 88.5$ MPa. Fig. 10 shows the averaged macroscopic stress–strain response in shear for the two SERVE's of Fig. 8. The results for the two SERVE's match very well with each other. This justifies the choice of $L_{SERVE} = 14$ μm.

II. Micromechanical SERVE analyses using the Voronoi cell FEM:

Solutions of the micromechanical boundary value problem in the SERVE are necessary to provide data for the AEH. This problem is posed in Eqs. (20)–(22), together with periodicity boundary condition on ∂Y and applied macroscopic strains. The

Voronoi cell finite element method or VCFEM, developed by Ghosh (2011), Moorthy and Ghosh (2000, 1998), Hu and Ghosh (2008) and Paquet and Ghosh (2011a) readily provides an accurate and efficient means for micromechanical analysis of deformation and failure in arbitrary heterogeneous microstructures. Morphological non-uniformities in dispersions, orientations, shapes, and sizes of inclusions are conveniently modeled by this method. In Paquet and Ghosh (2011a,b) the VCFEM model has been developed for rate-dependent elastic–viscoplastic porous ductile material. Micromechanical analysis in the present paper uses the VCFEM model in Paquet and Ghosh (2011a,b) with the void evolution facility switched off. The inclusions are linear elastic, while the matrix constitutive relations follow the over-stress model of Perzyna (1966) described in Section 3.

III. Computation of homogenized (level-2 microscopic) variables:

Homogenized quantities in Eqs. (23)–(27), used for the calibration of HCP model parameters for the inter-dendritic phase e.g. stress and strain tensors, are obtained by averaging the corresponding level-1 microscopic quantities over the SERVE:

$$\mathbf{\Sigma} = \frac{1}{Y}\int_Y \boldsymbol{\sigma}(\mathbf{y})\mathrm{d}Y; \quad \mathbf{e} = \frac{1}{Y}\int_Y \boldsymbol{\epsilon}(\mathbf{y})\mathrm{d}Y \tag{32}$$

where $\boldsymbol{\sigma}$ and $\boldsymbol{\epsilon}$ are the level-1 microscopic stress and strain tensors respectively. Additionally, the rate of plastic work (W_p) is defined as:

$$\dot{W}_p = \frac{1}{Y}\int_Y \boldsymbol{\sigma}(\mathbf{y}) : \dot{\boldsymbol{\epsilon}}^{\mathbf{p}}(\mathbf{y})\mathrm{d}Y \tag{33}$$

where $\boldsymbol{\epsilon}^{\mathbf{p}}$ is the level-1 microscopic plastic strain tensor.

4.2. Self-consistent homogenization for overall microstructure containing dendrites and inter-dendritic phases

The stage-2 homogenization in Fig. 2 is developed to evaluate the homogenized continuum plasticity (HCP) model for the cast aluminum alloy containing dendrites and inter-dendritic phases in the microstructure. The scale of the HCP model enables the calibration of model parameters by comparison with experimental data. A self-consistent homogenization (SCH) method is implemented for this stage due to the random dendrite cell distribution within the microstructure. Unlike the periodicity requirement for AEH, SCH assumes that the RVE is randomly distributed in a homogeneous material with the cast alloy properties.

The self-consistent method, originally developed in Budiansky (1965) and Hill (1965), estimates the overall material response by embedding a typical heterogeneity in an unbounded homogeneous material, with yet unknown macroscopic properties. The averaged response of each embedded phase is computed by solving a boundary value problem of the heterogeneous domain. The overall response of the aggregate is finally obtained by performing a volume average of the respective responses of each type of heterogeneity, as described in Nemat-Nasser and Hori (1999). The final properties correspond to those that satisfy consistency between the overall response of the aggregate and the volume averaged response in each phase.

4.2.1. Self-consistent homogenization for elastic–viscoplastic heterogeneous materials

The self-consistent method has been applied to isotropic viscoplastic materials in Stringfellow and Parks (1991). In the present paper, this model is extended to anisotropic elastic–viscoplastic materials. For stage-2 homogenization, the heterogeneous material contains two distinct phases, dendrites or inter-dendritic. Each phase $\alpha(=I,II)$ is an anisotropic elastic–viscoplastic material that can be described by the HCP model of Section 3. The constitutive relations within each phase α are written in a rate form as:

$$\dot{\boldsymbol{\sigma}}^{\alpha}(\mathbf{x}) = \mathbf{E}^{\alpha}_{\tan}(\mathbf{x}) : \dot{\boldsymbol{\epsilon}}^{\alpha}(\mathbf{x}) \quad \alpha = I, II \tag{34}$$

where $\mathbf{E}^{\alpha}_{\tan}$ is the local elastic–viscoplastic tangent modulus. Due to nonlinearity of the constitutive relations, $\mathbf{E}^{\alpha}_{\tan}$ can vary within each domain V_α occupied by αth phase. The homogenized response is obtained by assuming a random distribution of the two phases in a homogeneous equivalent medium. The overall behavior is also anisotropic elastic–viscoplastic with the constitutive behavior written as:

$$\dot{\mathbf{\Sigma}} = \mathbf{E}^{H}_{\tan} : \dot{\mathbf{e}} \tag{35}$$

where $\mathbf{\Sigma}$ and $\mathbf{e}$ are the macroscopic stress and strain tensors and $\mathbf{E}^{H}_{\tan}$ is the overall elastic–viscoplastic tangent modulus. For elliptical inclusions with constant tangent modulus, Eshelby has proved that the stress within the inclusion is constant (Eshelby, 1957). Furthermore, the strain in the αth phase can be related to the macroscopic applied strain through the relation (Chen and Argon, 1979):

$$\dot{\boldsymbol{\epsilon}}^{\alpha} = \mathbf{A}^{\alpha} : \dot{\mathbf{e}} \tag{36}$$

$\mathbf{A}$ is the fourth order strain-rate concentration tensor. The macroscopic tangent modulus $\mathbf{E}^{H}_{\tan}$ can be derived from the above relation.

For nonlinear materials for which the stresses and strains are nonuniform within a heterogeneity, the self-consistency condition is developed by generalization of the linear case following (Stringfellow and Parks, 1991). In this model, the inclusion stresses and strains are defined in terms of volume averages:

$$\dot{\boldsymbol{\epsilon}}^{\alpha} = \frac{1}{V_{\alpha}} \int_{V_{\alpha}} \dot{\boldsymbol{\epsilon}}(\mathbf{x}) \mathrm{d}V_{\alpha}; \quad \dot{\boldsymbol{\sigma}}^{\alpha} = \frac{1}{V_{\alpha}} \int_{V_{\alpha}} \dot{\boldsymbol{\sigma}}(\mathbf{x}) \mathrm{d}V_{\alpha} \tag{37}$$

The effective tangent modulus $\widehat{\mathbf{E}}^{\alpha}_{\mathrm{tan}}$ that relates the average stress and strain rates within phase α is defined by the relation:

$$\dot{\boldsymbol{\sigma}}^{\alpha} = \widehat{\mathbf{E}}^{\alpha}_{\mathrm{tan}} : \dot{\boldsymbol{\epsilon}}^{\alpha} \tag{38}$$

Self-consistency is enforced by requiring that the macroscopic fields are equal to volume-averages of the local fields, i.e.

$$\dot{\boldsymbol{\Sigma}} = \frac{1}{V} \int_{V} \dot{\boldsymbol{\sigma}}(\mathbf{x}) \mathrm{d}V = \sum_{\alpha=I}^{II} f_{\alpha} \dot{\boldsymbol{\sigma}}^{\alpha} \tag{39}$$

$$\dot{\mathbf{e}} = \frac{1}{V} \int_{V} \dot{\boldsymbol{\epsilon}}(\mathbf{x}) \mathrm{d}V = \sum_{\alpha=I}^{II} f_{\alpha} \dot{\boldsymbol{\epsilon}}^{\alpha} \tag{40}$$

where $f_{\alpha} = V_{\alpha}/V$ is the volume fraction of the phase α. The macroscopic tangent modulus $\mathbf{E}^{H}_{\mathrm{tan}}$ should be evaluated numerically.

4.2.2. Numerical implementation of the SCH for stage-2 homogenization

Stage-2 homogenization with self-consistent homogenization theory is used to obtain the overall elastic–viscoplastic behavior of the microstructure in Fig. 1(a). It uses results from stage-1 homogenization, where both pure matrix and inter-dendritic phase HCP model parameters are derived. An RVE, characterizing spatial distribution of the dendritic (pure aluminum) and inter-dendritic (aluminum with Si) phases in the microstructure, is embedded in a homogenized macroscopic material as shown in Fig. 11. Morphological information of the two phases is incorporated in a single model here, as opposed to conventional self-consistent procedures, where separate heterogeneities and boundary value problems are solved for each phase α. As in stage-1 homogenization, stage-2 homogenization consists of the following tasks.

I. Identification of the RVE:

A RVE must be identified for the SCH problem from Fig. 1(a). To execute this task, the microstructure in Fig. 11(a) is partitioned into two sub-regions, corresponding to the distributed phases of the pure aluminum matrix V_I and the inter-dendritic phase V_{II}. The equivalent RVE, representing an equivalent dendrite cell and its contiguous IDP, is shown in Fig. 11(b). It consists of a single ellipse representing the black matrix phase, embedded in the white outer box representing the IDP phase. The equivalent ellipse is obtained by equating the zero-*th*, first and second moments of area of all black dendrite cells in the pixelated image in Fig. 11(a) to the known moments for the ellipse. Details of this procedure are given in Li et al. (1999a,b). It results in the equivalence of volume fraction, centroidal location and orientation of the ellipse to the

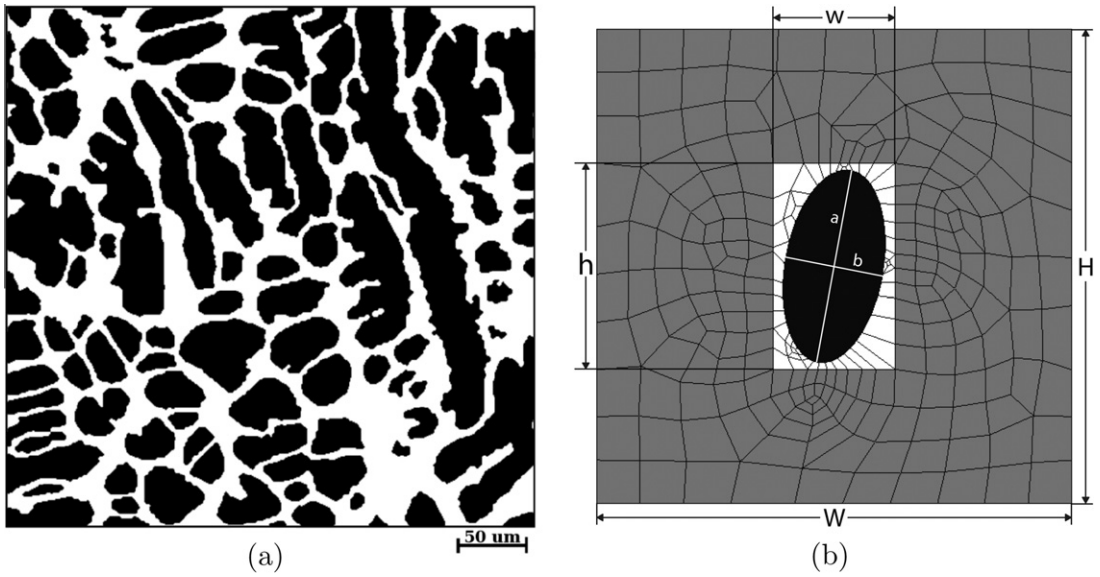

Fig. 11. (a) Simulated micrograph of Fig. 1(a) showing the distribution of pure aluminum matrix (black) and inter-dendritic (white) phases, (b) FEM mesh and model used for the self-consistent homogenization: pure matrix (black), inter-dendritic phase (white), and homogenized overall material (gray).

dispersed matrix phase in the microstructure. The area fraction of the aluminum matrix phase within the RVE is $f_I = 58.3\%$, while the aspect ratio and orientation (angle with the horizontal axis) of the equivalent ellipse are 1.98 and 80.36°, respectively. These geometrical parameters have been determined from a convergence study in which the size of the computational window extracted from the micrograph of Fig. 11(a) is varied. Results of the convergence study are shown in Fig. 12 for the computed area fraction, aspect ratio and orientation, normalized by their converged values. The outer rectangular box in Fig. 11(b) corresponds to the equivalent volume fractions of the IDP. The FEM model for the SCH consists of the RVE embedded in the homogeneous overall material, as shown in Fig. 11(b). The geometrical parameters of the self-consistent model are given in Table 2.

II. Micromechanical RVE analyses using conventional FEM:

Micromechanical analyses of the self-consistent homogenization RVE or SCH-RVE Fig. 11(b) are performed using the FEM software MSC-Nastran Marc, in which the rate-dependent HCP model is implemented using the user-defined subroutine *Uvscpl ()*. The stress update algorithm for the rate-dependent HCP model is based on the return mapping algorithm developed in Ghosh and Kikuchi (1988). FEM simulations are conducted to evaluate the HCP material parameters for the overall behavior of the dendritic microstructure using the parameters calibrated in stage-1 AEH. The HCP model parameters in Eqs. (3)–(5), for the matrix phase ($\alpha = I$) and the IDP ($\alpha = II$) are denoted in a vectorial form as:

$$\mathbf{p}_\alpha^1 = [\mathbf{C}^{\mathbf{e}}, Y_f(W_p), F(W_p), G(W_p), H(W_p), C(W_p), \Gamma_0, P]_\alpha^1 \tag{41}$$

Superscript 1 stands for stage-1 homogenization. It is important to note that the anisotropy parameters evolve with the averaged plastic work W_p defined in Eq. (33) due to constrained plastic flow in the microstructure. The macroscopic HCP model parameters $\mathbf{p}^2$ for stage-2 homogenization are computed by an iterative method described in Table 3.

III. Computation of homogenized (macroscopic) variables:

Calibration of the HCP material parameters requires the computation of homogenized quantities such as macroscopic stress $\boldsymbol{\Sigma}$ and strain $\mathbf{e}$. FEM generated microstructural variables in the SCH-RVE are integrated over the embedded RVE of Fig. 11(b), as:

$$\boldsymbol{\Sigma} = \frac{1}{V_I + V_{II}} \int_{RVE} \boldsymbol{\sigma}(\mathbf{y}) \mathrm{d}V = \sum_{\alpha=I}^{II} f_\alpha \boldsymbol{\sigma}^\alpha \tag{42}$$

$$\mathbf{e} = \frac{1}{V_I + V_{II}} \int_{RVE} \boldsymbol{\epsilon}(\mathbf{y}) \mathrm{d}V = \sum_{\alpha=I}^{II} f_\alpha \boldsymbol{\epsilon}^\alpha \tag{43}$$

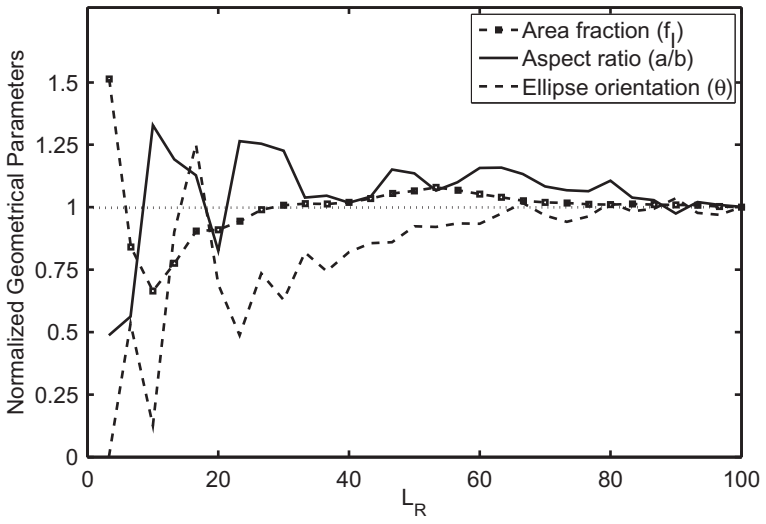

Fig. 12. Convergence of three different geometrical parameters in the FEM model as a function of the computational window size, expressed as $L_R = \frac{\text{length of computational window}}{\text{length of micrograph}} \times 100$.

Table 2
Geometrical parameters of the FEM model used for the self-consistent homogenization.

H	W	h	w	$2a$	$2b$	θ
30	30	13	7.7	12.13	6.12	80.36°

Table 3
Self-consistent homogenization algorithm for calibrating HCP parameters.

(1) Initialize HCP model parameters $\mathbf{p}^2$ by applying the mixture rule to $\mathbf{p}^1$ parameters, i.e.

$$\mathbf{p}^{2(0)} = f_I \mathbf{p}_I^1 + f_{II} \mathbf{p}_{II}^1$$

(2) Begin self-consistent homogenization (SCH) loop. Set $i = 0$
  (i) Conduct FEM simulation of the SCH-RVE model in Fig. 11(b) with parameters $\mathbf{p}^{2(i)}$
  (ii) Use Eqs. (42)–(44) to obtain homogenized material response
  (iii) Calibrate overall parameters $\mathbf{p}^{2(i+1)}$, following algorithm in Section 5.1
  (iv) Calculate error $e = \|\mathbf{p}^{2(i+1)} - \mathbf{p}^{2(i)}\|$
  (v) If $e \leqslant$ TOL exit, otherwise go to (i) for $i \leftarrow i + 1$
(3) Set homogenized material parameters $\mathbf{p}^2$ to $\mathbf{p}^{2(i)}$
(4) Conduct FEM simulation of the alloy with parameters $\mathbf{p}^2$

where $\boldsymbol{\sigma}^\alpha$ and $\boldsymbol{\epsilon}^\alpha$ are defined as in Eq. (37). V_I and V_{II} correspond to the areas of the aluminum matrix and the inter-dendritic phase, respectively. Additionally, the rate of plastic work (W_p) is computed as:

$$\dot{W}_p = \frac{1}{V_I + V_{II}} \int_{RVE} \boldsymbol{\sigma}(\mathbf{y}) : \dot{\boldsymbol{\epsilon}}^{\mathbf{p}}(\mathbf{y}) \, \mathrm{d}V \tag{44}$$

where $\boldsymbol{\epsilon}^{\mathbf{p}}$ is the plastic strain tensor in the level-2 microstructure.

5. Calibration of the HCP model parameters from experimental data

The nested dual-stage homogenization method is used to determine the HCP material parameters for modeling dendritic cast aluminum alloys from a limited experimental data set. Furthermore, it also evaluates the properties of the micro-constituents, viz. aluminum and Si particles. The iterative scheme, depicted in the nested structure of Fig. 2, has the following steps.

(1) The process starts with an initial guess for the material properties of micro-constituents, viz. the aluminum matrix and Si inclusions, denoted as $\mathbf{p}_{Al}^{(0)}$ and $\mathbf{p}_{Si}^{(0)}$, respectively. This initial guess is computed from the experimental data set using a simple mixture rule. The iterative process of the nested homogenization is then started, setting $i = 0$.
(2) Based on the asymptotic expansion homogenization (AEH) method of Section 4.1, LE-VCFEM micromechanical simulations of the SERVE in Fig. 8(c) are conducted to evaluate of the HCP material parameters $\mathbf{p}_{II}^{1(i)}$ of the inter-dendritic phase (IDP) from the micro-constituent properties $\mathbf{p}_{Al}^{(i)}$ and $\mathbf{p}_{Si}^{(i)}$. During this stage-1 homogenization, boundary value problems, posed in Eqs. (20)–(22), with periodicity boundary condition on ∂Y are solved for different applied strain paths using the numerical procedure developed in Ghosh et al. (2009). The material properties of the IDP are then evaluated from evolving homogenized variables, such as strains, stresses and inelastic work, obtained from Eqs. (32) and (33). The procedure used for the evaluation of the HCP parameters from these homogenized quantities is described in the subsequent Section 5.1. The HCP parameters of the pure matrix $\mathbf{p}_I^{1(i)}$ are also evaluated at this step. Since the dendritic-region is composed of a homogeneous aluminum matrix, parameters F_I^1, G_I^1, H_I^1 are equal to 0.5, and $C_I^1 = 3$.
(3) The sets of HCP parameters $\mathbf{p}_I^{1(i)}$ and $\mathbf{p}_{II}^{1(i)}$ calibrated in step 2 are used together with the self-consistent homogenization (SCH) scheme of Section 4.2 to evaluate the overall HCP material parameters of the alloy $\mathbf{p}^{2(i)}$, corresponding to the micro-constituent properties $\mathbf{p}_{Al}^{(i)}$ and $\mathbf{p}_{Si}^{(i)}$. Conventional FEM micromechanical boundary volume problems of the self-consistent model of Fig. 11(b) are solved using the algorithm in Table 3. Once the iterative self-consistent algorithm has converged, evolving homogenized quantities are computed using relations (42)–(44). The calibration of HCP material parameters $\mathbf{p}^{2(i)}$ from homogenized variables also follows the procedure described in Section 5.1.
(4) The macroscopic response predicted with the HCP model with parameters $\mathbf{p}^{2(i)}$ is compared to the experimental results in this step. An update is issued to the micro-constituent properties $\mathbf{p}_{Al}^{(i)}$ and $\mathbf{p}_{Si}^{(i)}$ by minimizing the error between the macroscopic response and the experimental data, defined in terms of the Frobenius norm of the difference in stress tensor, i.e.

$$\min_{\mathbf{p}_{Al}, \mathbf{p}_{Si}} \sum_{k=1}^{K} \left\| \left(\boldsymbol{\Sigma}^{\mathrm{HCP}}(\mathbf{p}_{Al}, \mathbf{p}_{Si})\right)^k - \left(\boldsymbol{\Sigma}^{\mathrm{exp}}\right)^k \right\|_F^2 \tag{45}$$

Here $\boldsymbol{\Sigma}^{\mathrm{HCP}}(\mathbf{p}_{Al}, \mathbf{p}_{Si})$ stands for the HCP response corresponding to micro-constituent properties $\mathbf{p}_{Al}^{(i)}$ and $\mathbf{p}_{Si}^{(i)}$. K is the total number of increments in the HCP simulation. The experimental response $(\Sigma^{\mathrm{exp}})^k$ corresponding the kth simulation increment is obtained by interpolating between experimentally recorded points. If the error lies within a prescribed

tolerance, the parameters $\mathbf{p}^2$ are set to $\mathbf{p}^{2(i)}$ and the nested algorithm is concluded. If not, the process continues and an update is issued to the properties $\mathbf{p}_{Al}^{(i)}$ and $\mathbf{p}_{Si}^{(i)}$ by minimizing Eq. (45) using a Newton–Raphson algorithm, i.e.

$$\mathbf{p}_{Al}^{(i+1)} = \mathbf{p}_{Al}^{(i)} + \delta\mathbf{p}_{Al}^{(i)}$$
$$\mathbf{p}_{Si}^{(i+1)} = \mathbf{p}_{Si}^{(i)} + \delta\mathbf{p}_{Si}^{(i)}$$

The iterative process continues by setting $i \leftarrow i+1$ and going back to step 2, till convergence is reached.

The method for evaluation of HCP material parameters from homogenized variables in steps 2 and 3 is described next.

5.1. Evaluation of rate-dependent HCP model parameters from homogenization data

The procedure of evaluating the HCP model parameters in both stages of the nested homogenization scheme is the same. They are obtained from homogenized quantities such as macroscopic strain $\mathbf{e}$, plastic strain $\mathbf{e}^{\mathbf{p}}$, stress $\boldsymbol{\Sigma}$ and plastic work W_p obtained from AEH in stage-1 or SCH in stage-2. The parameters are calibrated in the material principal coordinate system following the procedure outlined for rate-independent materials in Ghosh et al. (2009). These are discussed next. Prior to the calibration process, the fourth order anisotropic elasticity tensor $\mathbf{C}^{\mathbf{e}}$ is computed numerically by applying four independent macroscopic elastic strain increments, viz. $e_{xx} = \epsilon$; $e_{yy} = \epsilon$; $e_{zz} = \epsilon$; $e_{xy} = \epsilon$ on the unloaded RVE and by computing the resulting increment of the homogenized stress tensor. The generalized plane strain formulation developed in Hu and Ghosh (2008) and Paquet and Ghosh (2011a) is used to apply the strain increment $e_{zz} = \epsilon$.

(1) Yield stress $Y_f(W_p)$ and anisotropy parameter C:
The hardening behavior is described by the flow stress in shear $Y_f(W_p)$ that is a function of the plastic work W_p. Evolution of $Y_f(W_p)$ is calibrated by applying a rate-independent shear deformation to the microstructural RVE ($e_{xx} = e_{yy} = 0, e_{xy} \neq 0$). The resulting macroscopic stress tensor $\boldsymbol{\Sigma}$ is of the form $\Sigma_{xx} = \Sigma_{yy} = 0$, $\Sigma_{xy} \neq 0$ and the yield stress evolution is computed as:

$$Y_f(W_p) = \sqrt{3}\Sigma_{xy} \tag{46}$$

where the anisotropy parameter C is set to 3. This follows from the substitution $F = 0$ in Eq. (4) for the rate-independent case.

(2) Anisotropy parameters F, G, and H:
Functional forms of the anisotropy coefficients are calibrated from rate-independent simulations of the RVE under N loading conditions with different imposed strain ratios e_{xx}: e_{yy}: e_{xy}. At the end of each increment, the principal coordinate system is found and the corresponding macroscopic stress tensor $\boldsymbol{\Sigma}$ and plastic work W_p are computed. Plastic work dependent parameters $F(W_p)$, $G(W_p)$ and $H(W_p)$ are then calibrated by minimizing the square residual of the rate-independent form of Eq. (4) for all the loading conditions:

$$\min_{F,G,H} \sum_{i=1}^{N} \left[F\left(\Sigma_{yy}^i - \Sigma_{zz}^i\right)^2 + G\left(\Sigma_{zz}^i - \Sigma_{xx}^i\right)^2 + H\left(\Sigma_{xx}^i - \Sigma_{yy}^i\right)^2 + C\left(\Sigma_{xy}^i\right)^2 - \left(Y_f^i\right)^2 \right]^2 \tag{47}$$

$Y_f(W_p)$ is evaluated from the calibration results (1). A total of $N = 18$ different loading conditions are used in this work.

(3) Viscoplastic parameters Γ_0 and P:
The homogenized viscoplastic parameters in the HCP model are calibrated from a set of loading conditions combining N different imposed strain ratios e_{xx}: e_{yy}: e_{xy} and M applied strain rates for each loading. At each increment, the principal coordinate system, the stress tensor $\boldsymbol{\Sigma}$ and the plastic work W_p are computed. The corresponding yield stress $Y_f(W_p)$ and anisotropy coefficients $F(W_p)$, $G(W_p)$, $H(W_p)$ are evaluated using the previous calibration results. The macroscopic viscoplastic parameters are obtained by minimizing the square of the error between micromechanical analyses and macroscopic simulations using the HCP model of Section 3. The error is defined as the Frobenius norm of the stress difference:

$$\min_{\Gamma_0,P} \sum_{i=1}^{N} \sum_{j=1}^{M} \sum_{k=1}^{K_i} \left\| \boldsymbol{\Sigma}_{\text{macro}}^{ijk} - \boldsymbol{\Sigma}_{\text{micro}}^{ijk} \right\|_F^2 \tag{48}$$

where K_i is the number of applied increments in the simulations corresponding to the ith load path. For the calibration of viscoplastic parameters, four different strain rates in shear are applied, i.e. $N = 1$ and $M = 4$. The applied strain rates are $\dot{e}_{xy}^{(1)} = 0.01\ \text{s}^{-1}$, $\dot{e}_{xy}^{(2)} = 0.03\ \text{s}^{-1}$, $\dot{e}_{xy}^{(3)} = 0.06\ \text{s}^{-1}$ and $\dot{e}_{xy}^{(4)} = 0.10\ \text{s}^{-1}$.

6. Parameter calibration and modeling compression test of a cast aluminum alloy

The nested dual stage homogenization scheme is applied to calibrate material parameters and model the mechanical response of the cast aluminum alloy AS7GU of Fig. 1 having a SDAS of 30 μm. The experimental data for compression tests have been generated in the thesis (Chisaka, 2009). Elastic properties of silicon inclusions have been calibrated in Hu and Ghosh

(2008) as E_{Si} = 165 GPa and ν_{Si} = 0.27. Therefore the parameters and properties that will be calibrated by the iterative scheme are:

- micro-constituent properties of the pure matrix $\mathbf{p}_{Al}$
- overall HCP parameters of the matrix $\mathbf{p}_I^1$ and inter-dendritic phase $\mathbf{p}_{II}^1$
- overall HCP parameters of the cast alloy $\mathbf{p}^2$

Calibration of rate-independent and rate-dependent parameters is performed in two different steps that are described next.

6.1. Calibration of rate-independent material parameters

Rate-independent HCP model parameters of the alloy are calibrated from compression test data of Fig. 13 for an applied strain rate of $\dot{e}_{xx}^{(1)} = -0.01\ \mathrm{s}^{-1}$. Rate-independent properties for the isotropic aluminum matrix correspond to the plastic

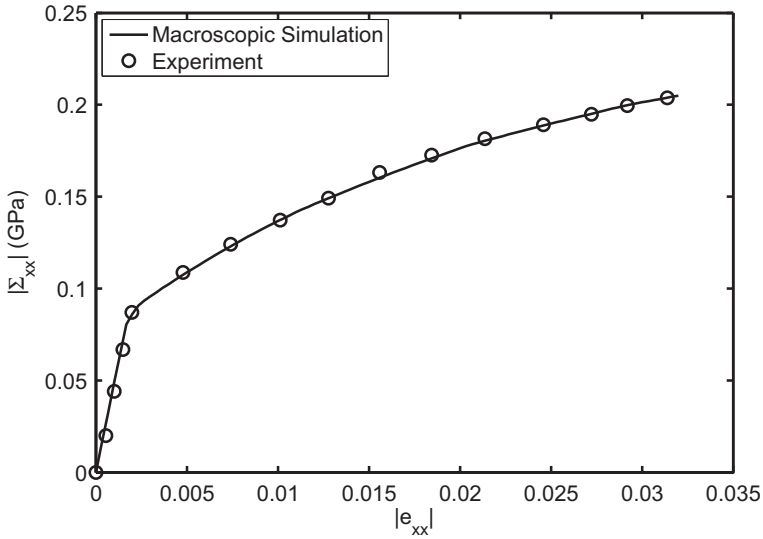

Fig. 13. Comparison of stress–strain response in compression by the HCP model with experimental data.

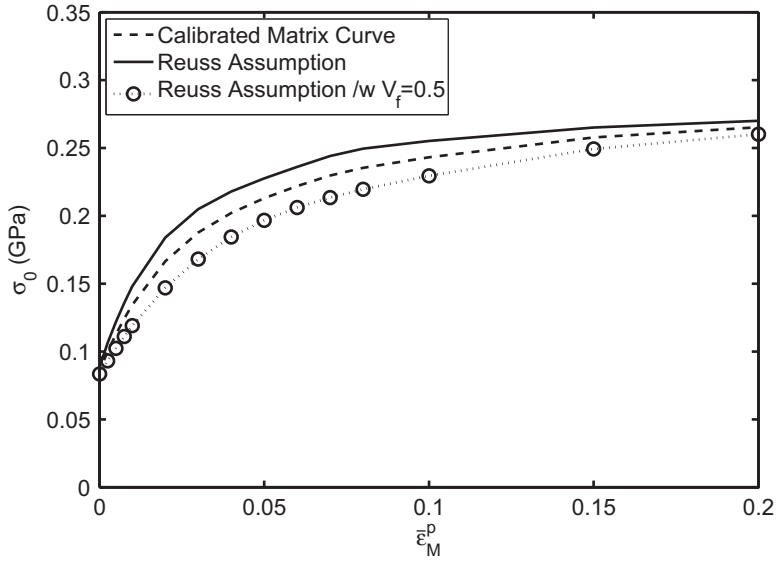

Fig. 14. Comparison of the calibrated plastic stress–strain curve $\sigma_0(\bar{\epsilon}_M^p)$ with the Reuss bounds $\sigma_0^{(1)}(\bar{\epsilon}_M^p)$ and $\sigma_0^{(2)}(\bar{\epsilon}_M^p)$.

hardening curve. The initial guess for the homogenization based iterative solution is obtained from experimental results using the Reuss upper bound. This initial guess, denoted by $\sigma_0^{(1)}(\bar{\epsilon}_M^p)$, is plotted in Fig. 14.

A lower estimate of the hardening curve, denoted by $\sigma_0^{(2)}(\bar{\epsilon}_M^p)$, is obtained by again using the Reuss homogenization but with a higher value of the inclusion volume fraction $V_f = 50\%$ instead of the actual value of $V_f = 7.3\%$. The corresponding plot is shown in Fig. 14. It is assumed that the actual hardening curve can be obtained by interpolating between these two values, i.e.:

$$\sigma_0(\bar{\epsilon}_M^p) = \chi\sigma_0^{(1)}(\bar{\epsilon}_M^p) + (1-\chi)\sigma_0^{(2)}(\bar{\epsilon}_M^p) \tag{49}$$

The determination of the actual hardening curve and hence the weighting function χ involves the iterative process described in Section 5, in which the error between predicted and experimental responses is minimized with respect to χ:

$$\min_{0\leqslant\chi\leqslant 1} \sum_{k=1}^{K} \left[\left(\Sigma_{xx}^{\mathrm{HCP}}(\chi)\right)^k - \left(\Sigma_{xx}^{\mathrm{exp}}\right)^k \right]^2 \tag{50}$$

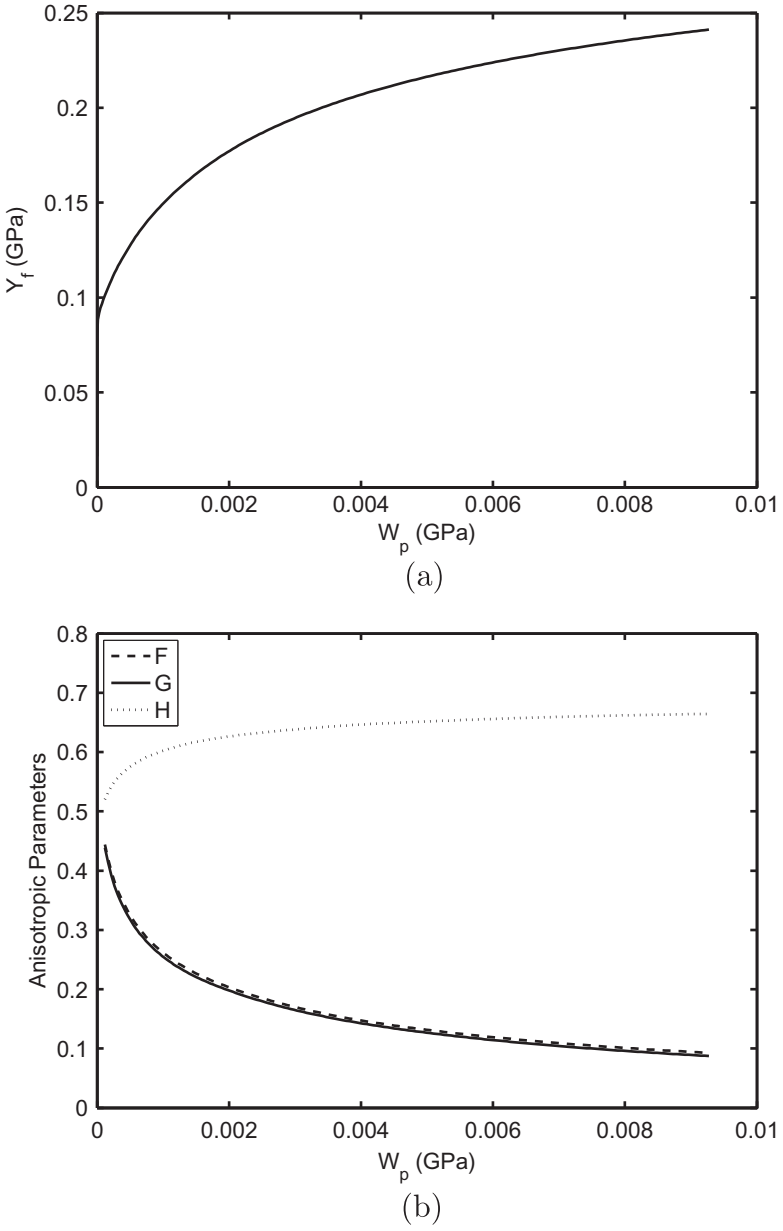

Fig. 15. Homogenized properties of inter-dendritic phase (IDP): (a) yield stress evolution, (b) evolution of anisotropy parameters *F*, *G*, and *H* with plastic work.

where $\Sigma_{xx}^{\mathrm{HCP}}(\chi)$ is the predicted response in compression for the overall cast alloy microstructure, using the hardening behavior $\sigma_0(\bar{\epsilon}_M^p)|_\chi$. $\Sigma_{xx}^{\mathrm{exp}}$ is the experimental response. K is the number of increments in the HCP simulation.

Minimization of Eq. (50) leads to $\chi = 0.451$. The corresponding plastic hardening behavior for the aluminum matrix is compared to the two bounds in Fig. 14. A comparison of the HCP model simulated results with the experimental data is shown in Fig. 13.

6.1.1. Rate-independent HCP parameters of the inter-dendritic phase

Fig. 15 shows the homogenized plastic hardening behavior of the inter-dendritic phase, as well as the evolution of anisotropy parameters $F_{II}^1, G_{II}^1, H_{II}^1$ with plastic work W_p. For comparison, the HCP material parameters of the pure aluminum matrix are shown in Fig. 16. It is important to note that the evolution of anisotropy parameters with plastic work is independent of the loading path. The presence of inclusions within the inter-dendritic phase significantly hardens its plastic behavior. The results of Fig. 15 show that the plastic behavior of the IDP is isotropic in the plane of the micrograph and that only an anisotropy related to the plane strain condition is observed. Functional forms are derived from a least square fit of the data in

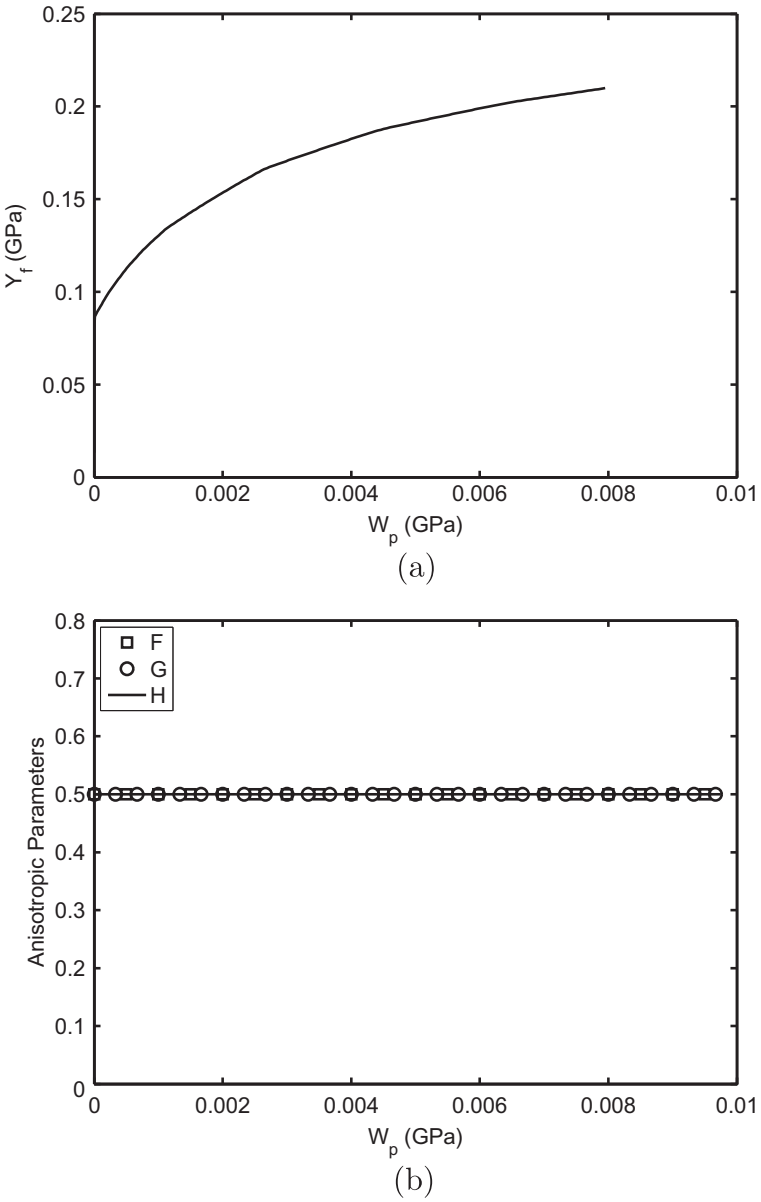

Fig. 16. Properties of the aluminum matrix: (a) yield stress evolution, (b) evolution of anisotropy parameters F, G, and H with plastic work.

Figs. 15 and 16 for the evolutions of the yield stress and anisotropy coefficients with inelastic work. These functionals and the corresponding correlation coefficients R^2 are reported in Table 4. A power relation is found between Y_f and W_p, while the evolution of anisotropy coefficients F, G and H is logarithmic.

Table 4
Calibrated HCP model rate-independent parameters for the matrix and inter-dendritic phase (IDP) from stage-1 (AEH) homogenization, and for the cast alloy microstructure from stage-2 (SCH) homogenization. Inelastic work W_p is expressed in GPa.

Materials	Y_f (GPa)	$F \sim G$	H	C
Matrix phase	$0.89W_p^{0.36} + 0.058 (R^2 = 0.995)$	0.5	0.5	3.0
Inter-dendritic phase (IDP)	$0.72W_p^{0.26} + 0.032 (R^2 = 0.994)$	$-0.080\ln(W_p) - 0.29$ (R^2 = 0.996)	$0.032\ln(W_p) + 0.82$ (R^2 = 0.985)	3.0
Cast alloy microstructure	$0.98W_p^{0.35} + 0.054 (R^2 = 0.998)$	$-0.032\ln(W_p) + 0.18$ (R^2 = 0.996)	$0.013\ln(W_p) + 0.63$ (R^2 = 0.985)	3.0

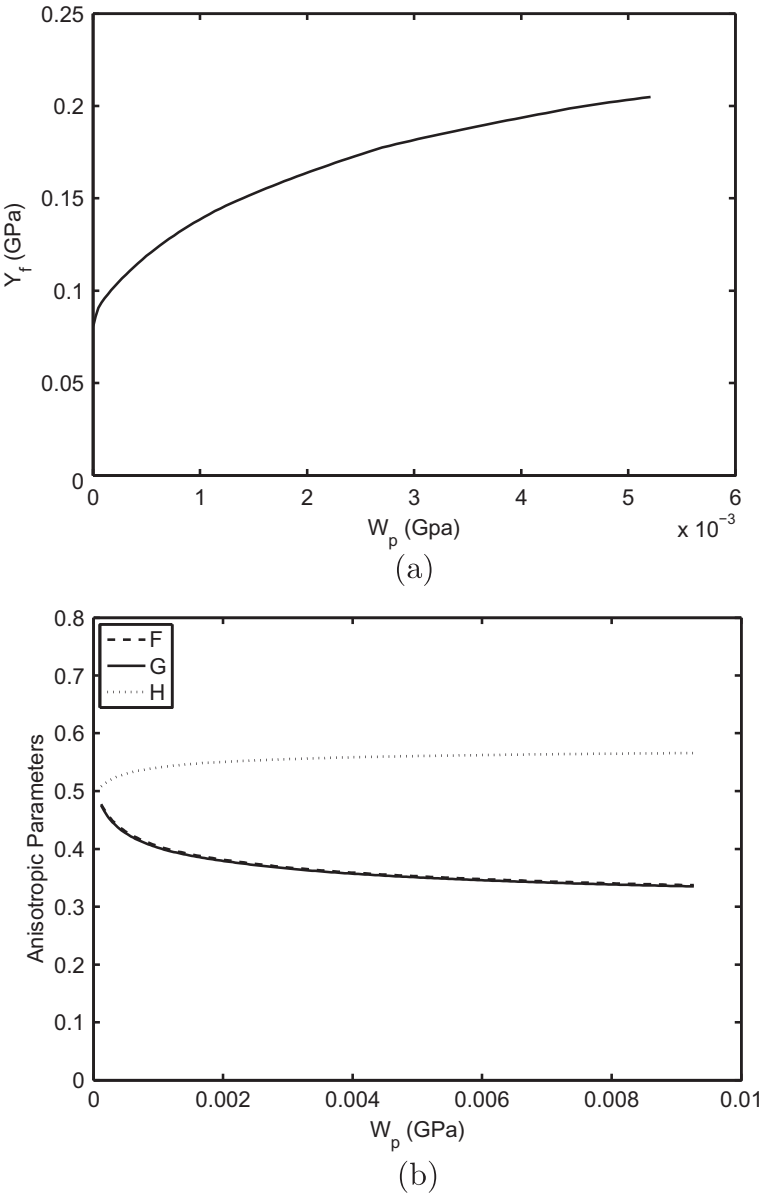

Fig. 17. Overall homogenized properties of the cast aluminum alloy: (a) yield stress evolution, (b) evolution of anisotropy parameters F, G, and H with plastic work.

6.1.2. Rate-independent overall properties of cast alloy

The calibrated overall hardening curve and anisotropy coefficients of the alloy AS7GU are shown in Fig. 17 and the corresponding functional forms are reported in Table 4. Fig. 18 compares the respective responses of the pure matrix and inter-dendritic phases with the overall response of the cast alloy in compression. Excellent match is observed between the experimental data and the simulated results in this figure.

6.2. Calibration of rate-dependent HCP model parameters

Rate-dependent material parameters are calibrated from the compression results for an applied strain rate of $\dot{e}_{xx}^{(2)} = -0.1\ \mathrm{s}^{-1}$. The viscoplastic parameters of the aluminum matrix γ_0 and p are determined by minimizing the error between predicted overall response and experimental results:

$$\min_{\gamma_0,p} \sum_{j=1}^{M} \sum_{k=1}^{K} \left[\left(\Sigma_{xx}^{\mathrm{HCP}}(\gamma_0, p) \right)^{jk} - \left(\Sigma_{xx}^{\mathrm{exp}} \right)^{jk} \right]^2 \tag{51}$$

where $\Sigma_{xx}^{\mathrm{HCP}}(\gamma_0, p)$ is the predicted response of the overall microstructure corresponding to the microstructural material parameters γ_0 and p, and $\Sigma_{xx}^{\mathrm{exp}}$ is the experimental response. $M = 2$ is the number of experimental strain rates used for the calibration and K is the number of increments in the HCP simulations. The experimental response $\left(\Sigma_{xx}^{\mathrm{exp}}\right)^{jk}$ corresponding to the kth simulation increment is found by interpolating between the experimental data points.

Initial guesses for γ_0 and p are required for the calibration scheme as described in Section 5. For this, the overall viscosity Γ_0 of the alloy is first determined by minimizing the error:

$$\min_{\Gamma_0} \sum_{j=1}^{M} \sum_{k=1}^{K} \left[\left(\Sigma_{xx}^{\mathrm{HCP}}(\Gamma_0) \right)^{jk} - \left(\Sigma_{xx}^{\mathrm{exp}} \right)^{jk} \right]^2 \tag{52}$$

Since only two experimental strain rates are available, a viscosity parameter Γ_0 can result for different values of exponent P. In this work $P = 1$ and minimization of Eq. (52) is conducted by only varying Γ_0. Minimization of Eq. (52) leads to $\Gamma_0 = 7.52\ \mathrm{GPa}^{-1}\ \mathrm{s}^{-1}$. A comparison of the predicted stress–strain curve with the experimental results is given in Fig. 19. Excellent agreement is found between the two results. From this result, an initial guess for the viscosity constant $\gamma_0^{(0)} = 8.13\ \mathrm{GPa}^{-1}\ \mathrm{s}^{-1}$ is computed using a simple mixture rule. The exponent is initialized to $p^{(0)} = 1$.

The nested dual-stage homogenization calibration scheme leads to the following viscoplastic material parameters for the matrix: $\gamma_0 = 8.08\ \mathrm{GPa}^{-1}\ \mathrm{s}^{-1}$ and $p = 1$. The corresponding HCP viscoplastic parameters of the inter-dendritic phase are $(\Gamma_0)_{II}^{\mathrm{I}} = 6.75\ \mathrm{GPa}^{-1}\ \mathrm{s}^{-1}$ and $P_{II}^{\mathrm{I}} = 1$. Table 5 lists the HCP model viscoplastic parameters calibrated for the matrix, inter-dendritic phase and overall microstructure. It can be noticed that the viscosity parameter Γ_0 decreases with an increase of the volume fraction of Si inclusions. Fig. 20 shows a comparison between the HCP model response of the inter-dendritic phase with LE-VCFEM micromechanics simulations for various shear strain rates: $\dot{e}_{xy}^{(1)} = 0.01\ \mathrm{s}^{-1}$, $\dot{e}_{xy}^{(2)} = 0.03\ \mathrm{s}^{-1}$, $\dot{e}_{xy}^{(3)} = 0.06\ \mathrm{s}^{-1}$, and $\dot{e}_{xy}^{(4)} = 0.10\ \mathrm{s}^{-1}$. The HCP results match very well with the micromechanics simulations. These results strongly justify the use of the rate-dependent HCP model of Section 3 to describe the overall behavior of heterogeneous rate-dependent materials.

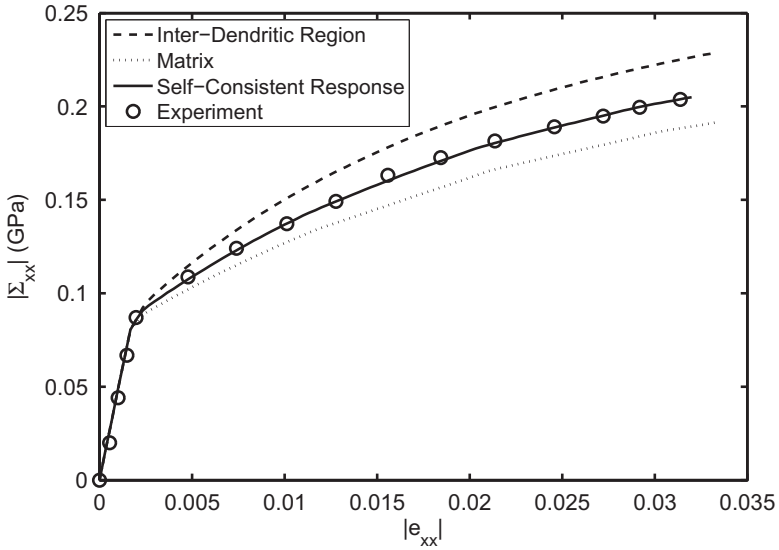

Fig. 18. Comparison of the self-consistent responses of the pure matrix, inter-dendritic phase, and the overall cast aluminum alloy in compression.

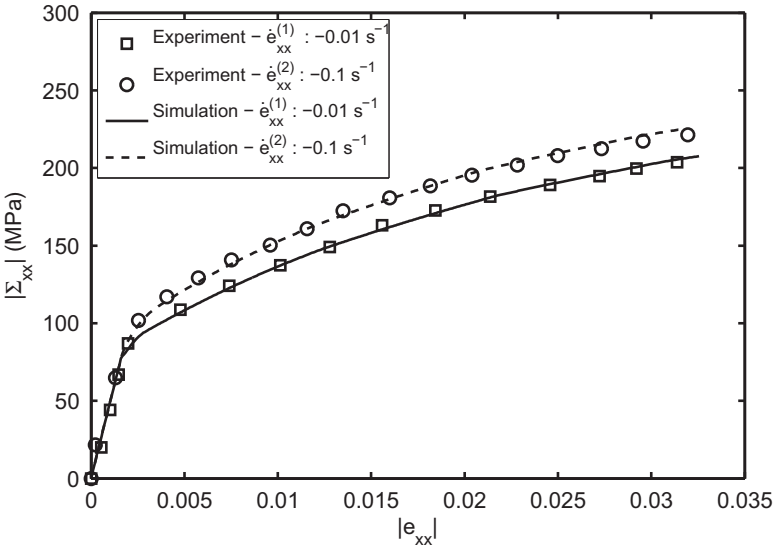

Fig. 19. Comparison of the HCP model response in compression with experimental data for the cast aluminum alloy at different strain rates.

Table 5
Calibrated HCP model viscoplastic parameters for the matrix and inter-dendritic phase (IDP) from stage-1 (AEH) homogenization, and for the cast alloy microstructure from stage-2 (SCH) homogenization.

Materials	V_f of Si (%)	Γ_0 (GPa^{-1} s^{-1})	P
Matrix phase	0.0	8.08	1
Inter-dendritic phase (IDP)	18.6	6.75	1
Cast alloy microstructure	7.3	7.52	1

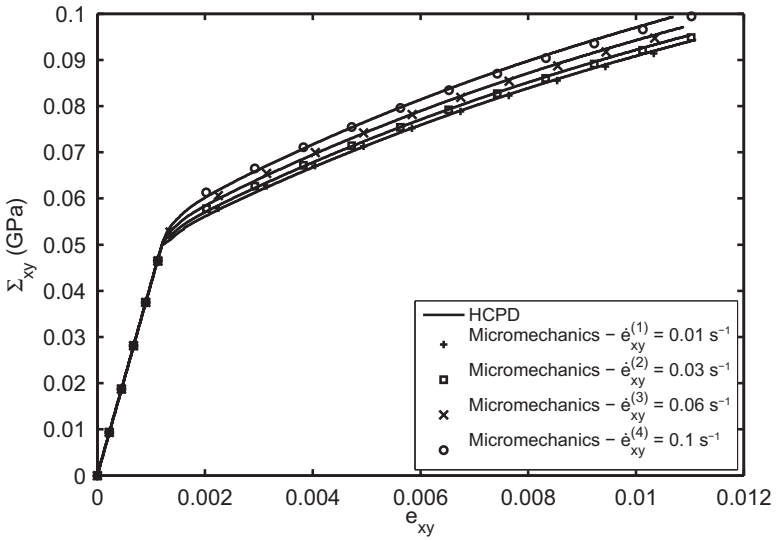

Fig. 20. Comparison of HCP model response for the inter-dendritic phase in shear for different strain rates with the micromechanics simulations.

7. Conclusions

This paper introduces a novel two-stage homogenization scheme to develop microstructure based continuum elasto–viscoplastic models for large SDAS cast aluminum alloys. The homogenization method is based on the inherent scales of inhomogeneity in the microstructure, thus overcoming limitations associated with one-step homogenization techniques that

require identification of a single RVE for the entire microstructure. Stage-1 homogenization is based on asymptotic expansion theory for obtaining the overall elastic–viscoplastic behavior of the inclusion-rich inter-dendritic phase. Stage-2 homogenization, which is based on the self-consistent method, is then performed to obtain the overall behavior of the cast alloy. Self-consistent homogenization embeds an RVE in an homogeneous material with yet unknown macroscopic material parameters. The two-stage homogenization requires identification of appropriate RVE's at each of the relevant length scales in the microstructure. The nested structure of the homogenization involves iteration. It enables evaluation of not only the overall homogenized model parameters of the cast alloy from experimental data, but also of constituents, such as inter-dendritic phase, aluminum matrix and Si inclusions. The multi-scale evaluation of multi-material properties is a unique feature that can provide a significant advantage with limited experimental data at fewer scales.

The homogenization based continuum plasticity (HCP) constitutive models for the inter-dendritic phase and the overall alloy are anisotropic and rate-dependent. The yield strength is modeled by the Hill's anisotropic yield function, while rate-dependency of plastic deformation is modeled using an over-stress model. Initial anisotropy is due to the distribution of heterogeneities like inclusions and dendrites. However this anisotropy evolves with deformation due to the constrained plastic flow in the microstructure. This evolution is captured in the HCP model through anisotropy parameters that evolve with deformation. The functional forms of the parameters overcome serious limitations of constant anisotropy parameters that are conventionally assumed in anisotropic models. Another unique feature is that the anisotropic HCP model is expressed with respect to the material principal coordinate system. This allows it to capture the effects of non-proportional load and deformation histories on the evolving anisotropy.

The potential of the rate-dependent HCP model is demonstrated for a cast aluminum alloy AS7GU having a SDAS of 30 μm. The nested dual-stage homogenization scheme is used to calibrate the viscoplastic parameters of the alloy. Excellent agreement is found between the predicted behavior of the cast aluminum alloy using the HCP model and compression experimental data. The extension of this work to rate-dependent HCP model for damaging porous ductile materials will be the subject of a future paper.

Acknowledgments

This work has been supported by the National Science Foundation NSF Div Civil and Mechanical Systems Division through the GOALI Grant No. CMS-0308666 (Program Director: Dr. G. Paulino), by the Department of Energy Aluminum Visions program through Grant No. A5997 and by the Army Research Office through Grant No. DAAD19-02-1-0428 (Program Director: Dr. B. Lamattina). This sponsorship is gratefully acknowledged. The authors are grateful to Drs. Steve Harris, John Allison, Xuming Su, and James Boileau of Ford Research Laboratory for invaluable discussions and for micrographs, samples and data used in this paper. Computer support by the Ohio Supercomputer Center through Grant PAS813-2 is also gratefully acknowledged.

References

Auriault, J.-L., 2002. Upscaling heterogeneous media by asymptotic expansions. J. Eng. Mech. 128, 817–822.
Benssousan, A., Lions, J.L., Papanicoulau, G., 1978. Asymptotic Analysis for Periodic Structures. North Holland, Amsterdam.
Benzerga, A.A., Besson, J., Pineau, A., 2004. Anisotropic ductile fracture, Part II: Theory. Acta Mater. 52, 4639–4650.
Budiansky, B., 1965. On the elastic moduli of some heterogeneous materials. J. Mech. Phys. Solids 13, 223–227.
Chen, I.W., Argon, A.S., 1979. Steady state power-law creep in heterogeneous alloys with coarse microstructures. Acta Metall. 27, 785–791.
Chisaka, K., December 2009. B.S. Thesis: Microstructure characterization and mechanical properties of cast aluminum alloy AS7GU, advisor: S. Ghosh, The Ohio State University.
Eshelby, J.D., 1957. The determination of the elastic field of an ellipsoidal inclusion, and related problems. Proc. Roy. Soc. A – Math. Phys. 241, 376–396.
Garajeu, M., Suquet, P., 1997. Effective properties of porous ideally plastic or viscoplastic materials containing rigid particles. J. Mech. Phys. Solids 45, 873–902.
Ghosh, S., 2011. Micromechanical Analysis and Multi-Scale Modeling Using the Voronoi Cell Finite Element Method. CRC Press, Taylor & Francis, Boca Raton, Fl.
Ghosh, S., Kikuchi, N., 1988. Finite element formulation for the simulation of hot sheet metal forming processes. Int. J. Eng. Sci. 26, 143–161.
Ghosh, S., Kikuchi, N., 1991. An arbitrary Lagrangian–Eulerian finite element method for large deformation analysis of elastic-viscoplastic solids. Comput. Methods Appl. Mech. Eng. 86, 127–188.
Ghosh, S., Mukhopadhyay, S., 1991. A two dimensional automatic mesh generator for finite element analysis of randomly dispersed composites. Comput. Struct. 41, 245–256.
Ghosh, S., Lee, K., Moorthy, S., 1995. Multiple scale analysis of heterogeneous elastic structures using homogenization theory and Voronoi cell finite element model. Int. J. Solids Struct. 32, 27–62.
Ghosh, S., Lee, K., Moorthy, S., 1996. Two scale analysis of heterogeneous elastic-plastic materials with asymptotic homogenization and Voronoi cell finite element model. Comput. Methods Appl. Mech. Eng. 132, 63–116.
Ghosh, S., Nowak, Z., Lee, K., 1997a. Quantitative characterization and modeling of composite microstructures by Voronoi cells. Acta Mater. 45, 2215–2234.
Ghosh, S., Nowak, Z., Lee, K., 1997b. Tesselation based computational methods for the characterization and analysis of heterogeneous microstructures. Compos. Sci. Technol. 57, 1187–1210.
Ghosh, S., Lee, K., Raghavan, P., 2001. A multi-level computational model for multi-scale damage analysis in composite and porous materials. Int. J. Solids Struct. 38, 2335–2385.
Ghosh, S., Valiveti, D.M., Harris, S.J., Boileau, J., 2006. A domain partitioning based pre-processor for multi-scale modeling of cast aluminum alloys. Modell. Simul. Mater. Sci. Eng. 14, 1363–1396.
Ghosh, S., Bai, J., Raghavan, P., 2007. Concurrent multi-level model for damage evolution in microstructurally debonding composites. Mech. Mater. 39, 241–266.
Ghosh, S., Bai, J., Paquet, D., 2009. Homogenization-based continuum plasticity-damage model for ductile failure of materials containing heterogeneities. J. Mech. Phys. Solids 57, 1017–1044.

Hill, R., 1948. A theory of yielding and plastic flow of anisotropic metals. Proc. Roy. Soc. A – Math. Phys. 193, 281–297.
Hill, R., 1965. A self-consistent mechanics of composite materials. J. Mech. Phys. Solids 13, 213–222.
Hu, C., Ghosh, S., 2008. Locally enhanced Voronoi cell finite element model (LE-VCFEM) for simulating evolving fracture in ductile microstructures containing inclusions. Int. J. Numer. Methods Eng. 76 (12), 1955–1992.
Liao, K., Pan, J., Tang, S., 1997. Approximate yield criterion for anisotropic porous ductile sheet metals. Mech. Mater. 26, 213–226.
Li, M., Ghosh, S., Richmond, O., Weiland, H., Rouns, T.N., 1999a. Three dimensional characterization and modeling of particle reinforced MMCs, Part I: Quantitative description of microstructural morphology. Mater. Sci. Eng. A 265, 153–173.
Li, M., Ghosh, S., Richmond, O., Weiland, H., Rouns, T.N., 1999b. Three dimensional characterization and modeling of particle reinforced MMCs, Part II: Damage characterization. Mater. Sci. Eng. A 266, 221–240.
Moorthy, S., Ghosh, S., 1998. A Voronoi cell finite element model for particle cracking in elastic–plastic composite materials. Comput. Methods Appl. Mech. Eng. 151, 377–400.
Moorthy, S., Ghosh, S., 2000. Adaptivity and convergence in the Voronoi cell finite element model for analyzing heterogeneous materials. Comput. Methods Appl. Mech. Eng. 185, 37–74.
Nemat-Nasser, S., Hori, M., 1999. Micromechanics: Overall Properties of Heterogeneous Materials. Elsevier. pp. 207–243.
Paquet, D., Ghosh, S., 2011a. Microstructural effects on ductile fracture in heterogeneous materials. Part I: Sensitivity analysis with LE-VCFEM. Eng. Fract. Mech. 78, 205–225.
Paquet, D., Ghosh, S., 2011b. Microstructural effects on ductile fracture in heterogeneous materials. Part II: Application to cast aluminum microstructures. Eng. Fract. Mech. 78, 226–233.
Perzyna, P., 1966. Fundamental problems in viscoplasticity. Adv. Appl. Mech. 9, 243–377.
Pyrz, R., 1994. Quantitative description of the microstructure of composites: I. Morphology of unidirectional composite systems. Compos. Sci. Technol. 50, 197–208.
Raghavan, P., Ghosh, S., 2004a. Adaptive multiscale modeling of composite materials. Comput. Model. Eng. Sci. 5 (2), 151–170.
Raghavan, P., Ghosh, S., 2004b. Concurrent multi-scale analysis of elastic composites by a multi-level computational model. Comput. Methods Appl. Mech. Eng. 193 (6–8), 497–538.
Sanchez-Palencia, E., 1983. Homogenization method for the study of composite media. In: Verhulst, F. (Ed.), Asymptotic Analysis II, Lecture Notes in Mathematics, vol. 985. Springer, Berlin, Heidelberg, pp. 192–214.
Stringfellow, R.G., Parks, D.M., 1991. A self-consistent model of isotropic viscoplastic behavior in multiphase materials. Int. J. Plast. 7, 529–547.
Swaminathan, S., Ghosh, S., 2006. Statistically equivalent representative volume elements for unidirectional composite microstructures: Part II – With damage. J. Compos. Mater. 40, 605–621.
Swaminathan, S., Ghosh, S., Pagano, N., 2006. Statistically equivalent representative volume elements for unidirectional composite microstructures: Part I – Without damage. J. Compos. Mater. 40, 583–604.
Wang, D., Pan, J., Liu, S., 2004. An anisotropic Gurson yield criterion for porous ductile sheet metals with planar anisotropy. Int. J. Damage Mech. 13, 7–33.